Kinematics of the outer accretion disk in cataclysmic variables

Paula Kvist

June 8, 2023

Abstract

This Masters thesis focuses on studying the kinematics of the outer accretion disk in cataclysmic variables. Cataclysmic variables are a type of interacting binary stars featuring a white dwarf and a main sequence star. Accretion disks in cataclysmic variables are born, when a secondary star still in main sequence overfills its Roche lobe and starts leaking gas towards the primary star (the white dwarf). The extent of the accretion disk has been a cause for discussion; methods measuring it from the hot spot, the place where accretion stream hits the disk, characteristically lead to smaller radii than measuring the radius from outer disk velocities. However, disk size estimates from the outer disk velocities heavily depend on the velocity field. The aim here is to check how close the outer accretion disk is to Keplerian velocities and simple three-body orbits. To do this, they are compared to simulated accretion disks using Smoothed Particle Hydrodynamics. Same comparisons are then done against observational data using Doppler tomography. Our study finds that the Keplerian velocity at the tidal truncation limit can safely be used as a lower limit for orbit-averaged disk. Furthermore, last non-intersecting three-body orbit seems to trace the disk edge quite well, and it can be used as an estimate for accretion disk size.

Contents

Introduction

Cataclysmic variables are a type of interacting binary stars, that have a white dwarf as a binary and a low-mass main sequence star as a secondary. The secondary star overfills its Roche lobe and leaks gas onto the primary. In this mass transfer process an accretion disk is formed, unless a strong magnetic field is present (Warner, 2003).

Accretion to a compact object is an efficient way to produce energy, and thus the accretion disk itself is a significant source of radiation in CVs. It outshines the secondary, and often is more prominent in spectra than the primary. Because of the low contribution of the stars to the luminosity and the spectra of cataclysmic variables, they are good subjects to the study of accretion processes (Frank et al., 2002).

Sometimes, within intervals of weeks to decades, an increase in accretion rate generates a sudden increase in luminosity, *an outburst*. Disks not in outburst are said to be *quiescent*. The gas in quiescent disks follow Keplerian orbits quite well in the inner parts, but some deviations are expected in outer disks due to, for example, gravitational pull of the secondary and irradiation pressure from the inner disk, primary and secondary. Indeed, the gas particles in outer disk are thought to follow three-body orbits.

This thesis intends to find out how much the particle velocities of three-body orbits actually deviate from circular Keplerian orbits, and from more sophisticated smoothed particle hydrodynamical simulations. Additionally, results from both of these simulations are compared to observations.

Chapter 1

Cataclysmic variables

1.1 Classification

Cataclysmic variables are classified based on their outburst behaviour. *Classical novae* have shown a single outburst in observable history, brightening from six magnitudes to up to almost 20 magnitudes before returning back to pre-outburst level. If a system has had several observed outbursts, it's classified as a *recurrent nova*. The outburst is caused by hydrogen-rich material that accretes on the surface of the primary. Once enough matter has accreted, it ignites a fusion reaction, leading to a thermonuclear runaway.

Dwarf novae have recurrent outbursts with intervals of dozens of days to some years. These outbursts are caused by changes in mass accretion rates, increasing the luminosity by 2-9 magnitudes. Historically, the difference between novae and dwarf novae was made by studying the outburst light curves. After the discovery of recurrent novae this method became problematic, as the time-scales and magnitudes of the outbursts can overlap between recurrent novae and dwarf novae. Thus, spectroscopic studies have been made to make further distinction between these groups. In classical and recurrent novae the outburst is powerful enough to eject a shell of disk material that is observable in their spectra. In dwarf novae no shell is lost.

Dwarf novae themselves have been further roughly classified into three categories, named after their archetype systems. *Z Cam* type stars have

standstills before they reach their maximum brightness. The standstills can last from days to years, after which they continue the outburst normally. *SU UMa* type systems experience superoutbursts that are brighter and last significantly longer than normal outbursts. Everything else is classified as *U Gem* type systems.

Systems where a strong magnetic field disrupt the accretion flow are called magnetic cataclysmic variables. They are classified into *polars* and *intermediate polars* based on the strength of the magnetic field. In these systems normal accretion disks are not formed, but different types of accretion columns and other flows can be found.

1.2 Observational characteristics

CVs radiate most of their light in visual wavelengths. In quiescence, most prominent spectral lines are Balmer series of hydrogen, neutral and singly ionized helium lines. Cooler outer disk parts mostly radiate with longer wavelengths, e.g. H_α, but the hot spot and hot inner disk emit higher Balmer lines and helium lines. Lines of metals such as calcium, magnesium and iron can be seen in some of the systems. The spectral lines originating from the accretion disk are double-peaked due to the rotational motion of the disc. In systems with low mass transfer rate the emission lines from accretion disk can be found in absorption dips originating from the primary. The shape of spectral line change with phase, as parts of the system eclipse another. In outburst the increase in continuum level outpower the emission lines, and absorption lines are observed instead.

Photometric observations often focus on forming light curves, or measuring the brightness of the object during an extended period of time. Information about system parameters, e.g. the separation of the stars, scale of an accretion disk, mass ratio and orbital period of the system can be extracted from light curves of eclipsing binaries. Additionally, the shape of light curve during an outburst can offer great insight to outburst phenomena.

The inclination of the system affect the observed data greatly. Edge-on systems show deep eclipses in light curves and spectra have well-defined

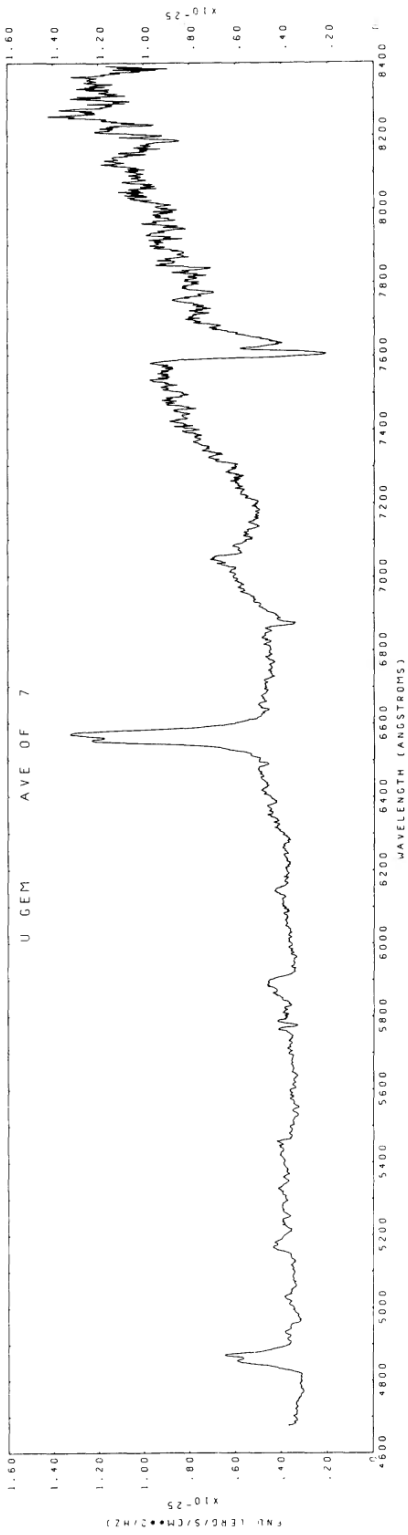

Figure 1.1: Spectrum of U Geminorum in quiescence. The H_α and H_β lines of Balmer series can be seen here at 6562.8 Å and 4861 Å, respectively. Flux rises near infrared wavelengths and TiO absorption from the secondary star can be seen (Stauffer et al., 1979).

double peaks. Systems that are more face-on can show very shallow eclipses and narrow peaks, and some systems show only single-peaked emission.

Chapter 2

Accretion disks

2.1 Roche surfaces

There are many applications in astronomy for situations where celestial bodies orbit so close to each other that one causes disruptions to its companion. The Roche problem, first studied by Edouard Roche, addresses a light test particle moving in a gravitational potential caused by two massive bodies, orbiting around their common center of mass. The model is based on three assumptions:

1. The massive bodies orbit each other in a circular orbit.

2. Stars co-rotate with the binary system.

3. The massive bodies are so centrally condensed that they can be described as point masses.

Luckily, this approach can justly be applied to cataclysmic variables, as all these assumptions hold reasonably well. Here we use a rotating coordinate system, where the primary star lies in the origin, x-axis connects the two stars and y-axis is perpendicular to x-axis. The total potential is now the combined effects of gravitational potential Φ_G of the stars (Frank et al., 2002;

Warner, 2003)

$$\Phi_G = -\frac{GM_1}{(x^2+y^2+z^2)^{1/2}} - \frac{GM_2}{((x-a)^2+y^2+z^2)^{1/2}} \tag{2.1}$$

and the effective potential of a centrifugal force Φ_c

$$\Phi_c = -\frac{1}{2}\left(\frac{2\pi}{P_{orb}}\right)^2 \left[\left(x - \frac{M_2}{M_1+M_2}a\right)^2 + y^2\right]. \tag{2.2}$$

Here G is the gravitatonal constant, M_1 and M_2 are the masses of the primary and secondary star respectively, x, y and z are the coordinates of the test particle, a is the separation of the stars and P_{orb} is the orbital period of the system.

Using Newton's generalization of Kepler's third law

$$P_{orb}^2 = \frac{4\pi^2 a^3}{G(M_1+M_2)}, \tag{2.3}$$

total potential of the test particle Φ_R is then

$$\Phi_R = -\frac{GM_1}{(x^2+y^2+z^2)^{1/2}} - \frac{GM_2}{((x-a)^2+y^2+z^2)^{1/2}} - \frac{1}{2}\frac{G(M_1+M_2)}{a^3}\left[\left(x - \frac{M_2}{M_1+M_2}a\right)^2 + y^2\right]. \tag{2.4}$$

The surface forming a constant potential is called an *equipotential surface*. Close to a star, the equipotential surfaces (at $z = 0$) are circular, but moving further away the shape becomes more elongated and encapsulates both stars. The separation of the stars a dictates the size of these surfaces while not changing the shape. The shape is determined by the mass ratio $q = M_2/M_1$ of the system. These equipotential surfaces are demonstrated in Fig. 2.1.

The equipotential surfaces that form lobes around the stars so that the lobes connect at the inner Lagrangian point $\mathcal{L}_1$ are called the *Roche lobes* of the stars. When the secondary star approaches its Roche lobe, it becomes significantly distorted and elongates towards the primary. If the secondary

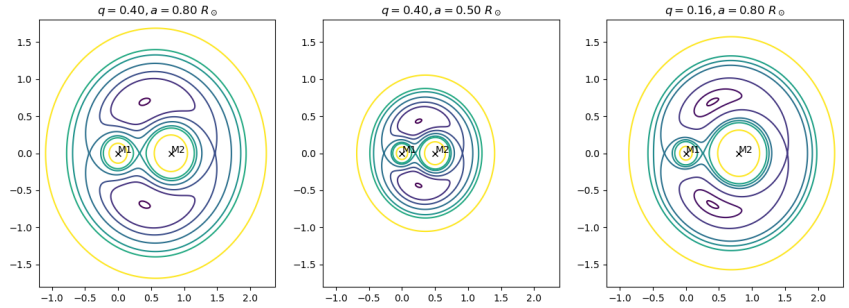

Figure 2.1: Equipotential surfaces with slightly different parameters. Left: $q = 0.4, a = 0.8$. Center: $q = 0.4, a = 0.5$. Right: $q = 0.16, a = 0.8$.

overfills its Roche lobe, the material is no longer bound to it but leaks gas to the primary. The gas flows with thermal velocities through $\mathcal{L}_1$ (Lubow and Shu, 1975).

There are several ways for an initially detached star to start losing mass. For example, a main-sequence star could evolve into a giant, grow its radius outside its Roche lobe and start leaking matter. On the other hand, as binary system evolves the stars spiral slowly towards each other due to angular momentum leaving the system with, e.g., stellar winds and gravitational radiation. This process shrinks the Roche lobe of the secondary star and grows the lobe of the primary star, as the distance a becomes shorter and mass ratio q becomes larger. After enough time, the Roche lobe of one star (or both) can shrink enough for it to start losing matter.

Because the geometry of a tidally-elongated lobe is difficult to work with, it is common to define *volume radius* of the Roche lobe. The volume radius is the radius of a sphere containing equal volume to the Roche lobe. Usual approximation for the Roche lobe of the secondary R_2 is (Eggleton, 1983):

$$\frac{R_2}{a} = \frac{0.49q^{2/3}}{0.6q^{2/3} + \ln\left(1 + q^{1/3}\right)}. \tag{2.5}$$

This equation is valid for any value $q > 0$, and is accurate to 1%.

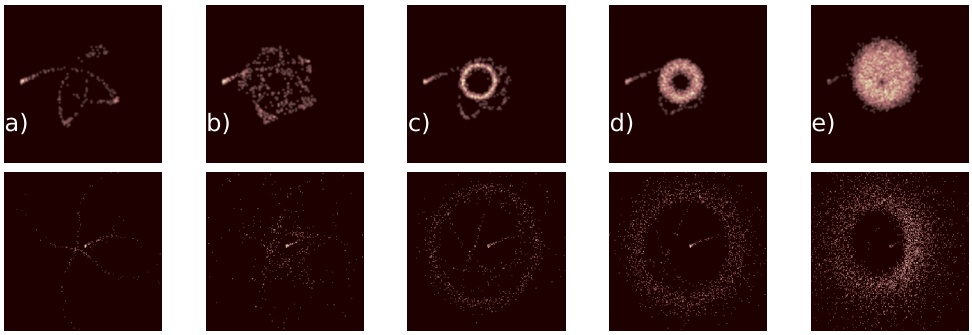

Figure 2.2: Simulated formation of an accretion disk in position (top) and velocity (bottom) coordinates. a) Three-body particle trajectories. b) Trajectories interact and dissipate. c) Initial accretion ring starts to form. d) Accretion ring dissipates and spreads to a disk. e) Accretion disk is born.

2.2 Formation of an accretion disk

The formation of an accretion disk is mostly governed by angular momentum conservation. The gas leaving the secondary star has some leftover angular momentum due to the rotation of the binary system. The gas travels through $\mathcal{L}_1$ and continues forward following trajectories well approximated by restricted three-body problem. The closest approach r_{min} of the gas stream to the primary star can be evaluated from Lubow and Shu (1975):

$$\frac{r_{min}}{a} = 0.0488q^{-0.464} \qquad 0.05 < q < 1 \tag{2.6}$$

If r_{min} is larger than the radius of the primary star, the gas does not hit the surface of the star but passes it instead. This is indeed the case for most cataclysmic variables.

As mentioned above, the gas particles are assumed to follow three-body trajectories while conserving the sum of kinetic and potential energy:

$$\frac{1}{2}\dot{r}^2 + \Phi_R = \text{const.} \tag{2.7}$$

A particle that has zero velocity at the Roche lobe of the primary cannot escape it at any point. Thus, Roche lobes have an additional name of *zero-velocity surfaces*. When a test particle reaches the zero-velocity surface,

it's kinetic energy is transferred into potential energy, thus it slows down until all it's energy is potential energy. There the gravitational pull of the start starts accelerating it back towards the primary. This initial stream will eventually turn into an accretion ring with Keplerian velocities due to thermal dissipation from the collision area. The *circularization radius* of this ring is (Lubow and Shu, 1975; Hessman and Hopp, 1990)

$$\frac{R_{ring}}{a} = 0.0859q^{-0.426} \qquad 0.05 \leq q < 1 \tag{2.8}$$

The initial ring rotates differentially, so the gas particles interact with each other, causing some of the particles to lose energy and sink deeper towards the primary. Due to the angular momentum conservation, other particles must move outwards, and the initial ring will spread into an accretion disk. The process of accretion disk formation is visualized in Figure 2.2.

2.3 Steady thin disk

A geometrically thin accretion disk is often described in cylindrical coordinates with following equations for mass and angular momentum conservation (Frank et al., 2002):

$$\frac{\partial \Sigma}{\partial t} = -\frac{1}{r}\frac{\partial}{\partial r}(r\Sigma v_r) \tag{2.9}$$

$$r\frac{\partial}{\partial t}\Sigma r^2\Omega + \frac{\partial}{\partial r}r\Sigma v_r r^2\Omega = \frac{1}{2\pi}\frac{\partial T}{\partial r} \tag{2.10}$$

Here r is the radius, t is time, v_r is the radial velocity of the disk, and Ω is the angular velocity, often assumed to have Keplerian value

$$\Omega = \Omega_K = \sqrt{\frac{GM_1}{r^3}}, \tag{2.11}$$

Σ is the column surface density as a function of density ρ and height z

$$\Sigma = 2\int_0^\infty \rho dz, \tag{2.12}$$

and T is torque with ν notating kinematic viscosity of the gas.

$$T(r,t) = 2\pi r\nu\Sigma r^2 \frac{d\Omega}{dr}. \tag{2.13}$$

Now, using 2.9, 2.10 and 2.13, we get an equation for the time evolution of surface density in a Keplerian accretion disk.

$$\frac{\partial\Sigma}{\partial t} = \frac{3}{r}\frac{\partial}{\partial r}\left(\sqrt{r}\frac{\partial}{\partial r}\nu\Sigma\sqrt{r}\right) \tag{2.14}$$

This equation is non-linear, as the function ν is not defined - it could be a function of r.

How valid is the assumption of the disk being thin? If there's no flow of matter in z-direction, the equation of hydrostatic equilibrium, when $z << r$, is

$$\frac{1}{\rho}\frac{\partial P}{\partial z} = \frac{\partial}{\partial z}\left(\frac{GM_1}{\sqrt{r^2+z^2}}\right) \approx -\frac{GM_1 z}{r^3}. \tag{2.15}$$

Here P means pressure. For a thin disk, the scale height $H \sim z$ should be much smaller than the radius r. Approximating $\partial P/\partial z \sim P/H$ and $P \sim \rho c_s^2$, where c_s is the sound speed, this condition is then

$$H \ll c_s\sqrt{\frac{r}{GM_1}}r \tag{2.16}$$

$$\Rightarrow c_s \ll \sqrt{\frac{GM_1}{r}} \tag{2.17}$$

So, for the thin disk approximation to be valid, the local Keplerian velocity should be much more than local sound speed c_s, which is indeed the case in accretion disks. Typical rotation velocities for the gas is of the order of 1000 km/s, while sound speed is normally of the order of 10 km/s. This approximation simplifies solving the disk structure remarkably: instead of solving the structure both radially and vertically, the problem can be transformed

into one dimension and known equations of stellar structure can be applied (Frank et al., 2002).

$$1.\ \rho = \frac{\Sigma}{H} \tag{2.18}$$

$$2.\ H = \frac{c_s r^{3/2}}{(GM)^{1/2}} \tag{2.19}$$

$$3.\ c_s^2 = \frac{P}{\rho} \tag{2.20}$$

$$4.\ P = \frac{\rho k T_c}{\mu m_p} + \frac{4\sigma}{3c} T_c^4 \tag{2.21}$$

$$5.\ \frac{4\sigma T_c^4}{3\tau} = \frac{3GM\dot{M}}{8\pi r^3}\left(1 - \left(\frac{r_1}{r}\right)^{1/2}\right) \tag{2.22}$$

$$6.\ \tau = \Sigma \kappa_R(\rho, T_c) \tag{2.23}$$

$$7.\ \nu\Sigma = \frac{\dot{M}}{3\pi}\left(1 - \left(\frac{r_1}{r}\right)^{1/2}\right) \tag{2.24}$$

$$8.\ \nu = \nu(\rho, T_c, \Sigma, \alpha, ...) \tag{2.25}$$

Here T_c is the central temperature, k is the Boltzmann constant, μ is the average mass of particles, m_p is the proton mass, σ is the Stefan-Boltzmann constant, c is the speed of light and τ is the optical depth and κ_R is the Rosseland mean opacity. α stands for a viscosity parameter, further to be discussed in the next chapter. The standard model for accretion disks is based on this prescription. Assuming that the radiation pressure is negligible, Kramer's law holds and Rosseland mean opacity is

$$\kappa_R = 5 \cdot 10^{24} \rho T_c^{-7/2} \mathrm{cm}^2 \mathrm{g}^{-1}. \tag{2.26}$$

The disc solution in cgs units, where R_{10} is the radius in units 10^{10} and $\dot{M}_{16}$

is the mass loss rate in units 10^{16}, becomes

$$\Sigma = 5.2\alpha^{4/5}\dot{M}_{16}^{7/10}m_1^{1/4}R_{10}^{-3/4}f^{14/5}\text{g cm}^{-2} \tag{2.27}$$

$$H = 1.7\cdot 10^{8}\alpha^{-1/10}\dot{M}_{16}^{3/20}m_1^{-3/8}R_{10}^{9/8}f^{3/5}\text{cm} \tag{2.28}$$

$$\rho = 3.1\cdot 10^{-8}\alpha^{-7/10}\dot{M}_{16}^{11/20}m_1^{5/8}R_{10}^{-15/8}f^{11/5}\text{g cm}^{-3} \tag{2.29}$$

$$T_c = 1.4\cdot 10^{4}\alpha^{-1/5}\dot{M}_{16}^{3/10}m_1^{1/4}R_{10}^{-3/4}f^{6/5}\text{K} \tag{2.30}$$

$$\tau = 190\alpha^{-4/5}\dot{M}_{16}^{1/5}f^{4/5} \tag{2.31}$$

$$\nu = 1.8\cdot 10^{14}\alpha^{4/5}\dot{M}_{16}^{3/10}m_1^{-1/4}R_{10}^{3/4}f^{6/5}\text{cm}^2\text{s}^{-1} \tag{2.32}$$

$$v_r = 2.7\cdot 10^{4}\alpha^{4/5}\dot{M}_{16}^{3/10}m_1^{-1/4}R_{10}^{-1/4}f^{-14/5}\text{cm s}^{-}1 \tag{2.33}$$

$$f = \left[1-\left(\frac{R_*}{R}\right)^{1/2}\right]^{1/4} \tag{2.34}$$

The main problem with this model is the unknown nature of α: it could be a function of radius, mass transfer rate or mass itself; luckily the quantities do not depend too much on α.

2.4 Viscosity

An angular momentum transfer mechanism must exist to allow aforementioned disk formation and accretion. As the exact mechanism in accretion disks is still a matter of discussion, it is masked behind viscosity.

For over 50 years the theory of accretion disks has been built on the α-disk model by Shakura and Sunyaev (1973), where the unknown nature of the viscosity is hidden inside a parameter α. Here, the viscosity ν is

$$\nu = \alpha c_s H. \tag{2.35}$$

Here we mainly assume that the turbulent eddies are of the size or smaller than the disk scale height and that the turnover velocity is smaller than sound speed. The unknown in viscosity is now transferred from ν to α, and an estimate that α is likely smaller than 1 is gained.

Some estimates of the values of α have been obtained from observations; expected values are roughly $\alpha \sim 0.01$ in quiescence and $\alpha \sim 0.1 - 0.3$ in outburst (Cannizzo, 1993; Kotko and Lasota, 2012). The strongest candidates behind viscosity nowadays include magnetorotational instability theory (Balbus and Hawley, 1991) and spiral shocks excited by a non-axisymmetrical gravitational potential (Sawada et al., 1986). They both could explain a mechanism for angular momentum transfer, which is essential to allow gas to accrete towards the primary in the first place.

Magnetorotational instability (MRI) is now widely recognized as the driver behind angular momentum transfer. A study by Balbus and Hawley (1991) found that a weak magnetic field causes instability in disks where the angular velocity decreases radially outwards. Here two particles originally on the same magnetic field line will be a subject to two forces: magnetic tension between the particles, trying to slow down the inner particle and speed up the outer particle, and gravity trying to speed up the inner particle falling towards the primary. This process introduces a rapidly growing instability leading in turbulence, allowing angular momentum to be transferred outwards.

Numerical simulations have been made both locally and globally. Local simulations (e.g. Papaloizou and Lin, 1995) typically use some shearing-box models with Keplerian flows, trying to solve how a small magnetic field affects a flow in a single part of the disk. Global simulations (e.g. Sorathia et al., 2012) try to simulate how the disks behave in larger scales, acknowledging the cylindrical or circular coordinates. Global simulations are more extensive computationally, so more work has been done concerning local models of MRI. One major concern of this model is that the amount of angular momentum transferred decreases with increasing resolution in numerical simulations (Fromang and Papaloizou, 2007).

The perturbations of the secondary star in the orbits of gas particles are seen as inward-propagating waves (Goldreich and Tremaine, 1978; Lubow, 1991). Numerical simulations have shown that these waves take the form of spiral arms (e.g., Yukawa et al., 1997; Makita et al., 2000). The spiral arms rotate slower than the general gas bulk in the accretion disk, and when

the velocity difference gets larger than the local sound speed, causes non-linear shocks. The shock fronts result in locally negative angular momentum, allowing the disk to transfer angular momentum outwards (Papaloizou and Lin, 1995). Spiral arms have already been observed in many system during last couple of decades, including IP Peg, UX UMa and SS Cyg (Baptista et al., 2005; Neustroev et al., 2011).

In recent years 3D global magnetohydrodynamical studies have been made about the combined effects of spiral arms and magnetorotational instability. Ju et al. (2017) found that with relatively low Mach numbers (of the order of 10) and gas to magnetic pressure ratio of 400 spiral shocks can transfer about the same amount of angular momentum as MRI. This explanation might provide additional transportation mechanism needed by quiescent disks, as MRI is not as efficient in unionized gas. However, the simulations were done using simplistic temperature profiles (adiabatic and isothermal), and the Mach number used is lower than typical values in accretion disks ($M \sim 100$, for an order of magnitude estimate). The efficiency of spiral shocks lowered with increasing Mach number in the simulations.

2.5 Disk instability model

The modern understanding of outburst behaviour in dwarf novae concern a thermal instability arising at the ionization temperature of hydrogen (Lasota, 2001). As the disk is in low-viscosity quiescent state, hydrogen is mostly neutral. As the matter accumulates in the disk, its temperature rises until it is high enough to partially ionize hydrogen. The freed electrons cause the opacity of the disk to rise, causing rising viscosity and heating the disk even more. The material in the disk starts to flow faster and faster towards the primary, leading to an outburst. At some point, the mass transfer rate in the disk exceeds the mass transfer rate from the secondary, the disk starts to cool down, temperature lowers under the ionization temperature of hydrogen and the disk declines back in to quiescent state.

The essence of disk instability model can be visualized with the S-curve (Fig. 2.3). A disk in the lower line is cold and in quiescence. The upper line

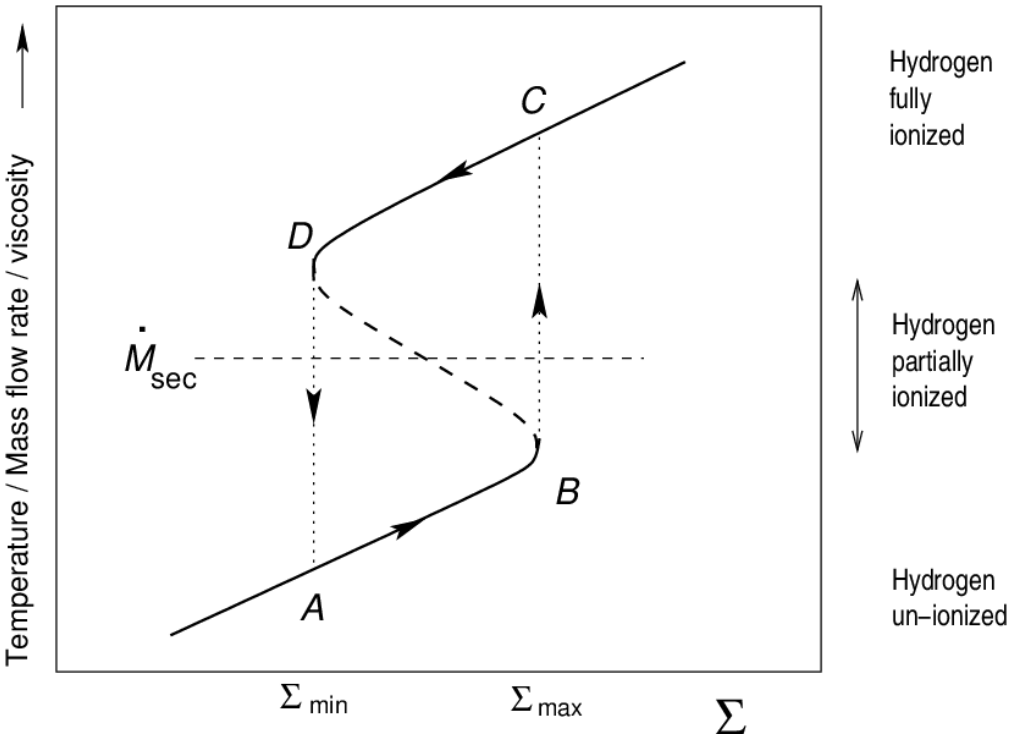

Figure 2.3: Temperature of an accretion disk as a function of surface density. S-curve is formed, with the disk in cold state at the bottom and hot state at the top. Between them stays a unstable region Lasota (2001).

represents hot disk in outburst. Between these two stable states is a region where the disk is unstable. A thermal limit cycle is formed: once enough matter has accumulated in the cold disk that the surface density passes Σ_{max}, the disk temperature rises rapidly above the ionization temperature of hydrogen and the disk switches to hot state. There its viscosity rises, material accretes faster and luminosity increases; this is observed as an outburst. After some time the disk starts to cool down. Once the surface density has thinned out to Σ_{min}, the disk switches rapidly to cold state and the cycle starts over.

2.6 Size of an accretion disk

At large enough distance from the primary, the tidal forces caused by the secondary start to distort the orbits of the particles. The orbits start to

deviate from circular and elongate towards the secondary, making the orbits egg-shaped. Paczynski (1977) calculated last non-intersecting orbits using single-particle three-body simulations. The results can be approximated by Neustroev and Zharikov (2020):

$$\frac{R_d}{a} = 0.353 + 0.271\mathrm{e}^{-3.045q}, \qquad 0.03 < q < 0.73. \tag{2.36}$$

After this orbit the tidal shear will produce enough dissipation to prevent the disk from growing any larger. However, in real systems phenomena including e.g. pressure terms and viscosity could allow the disk to grow slightly over this radius (Neustroev and Zharikov, 2020).

Several utilized radius measurement methods rely on measuring light curves. For example in eclipse contact timing (Sulkanen et al., 1981), disk eclipse widths are measured from light curves and disk radius is simply calculated from the eclipse width. Eclipse mapping, developed by Horne (1985), takes this method a bit further by producing model light curves and adjusting parameters until they match observed ones. Both of these methods rely on the assumption that the hot spot, a part of the disk producing most radiation, is at the edge of the disk. However, as it became evident that the outer disk can extend beyond the observable hot spot (e.g. Skidmore et al. 2000), other methods should be used.

A given point in an accretion disk can be defined by its spatial position, or more usefully by its velocity, as the velocity of a particle is reflected in spectra of the system. As the accretion disk rotates, the particles moving away from the line-of-sight of the observer are slightly red-shifted, and the particles moving towards the observer are slightly blue-shifted. This results in the characteristic double-peaked line profile of accretion disk emission lines. As the binary itself rotates, different parts of the system have slightly different velocities: for example, the emission from the hot spot travels from the blue wing of the spectrum to the red wing and then back. For an observer the velocity shift can be calculated from

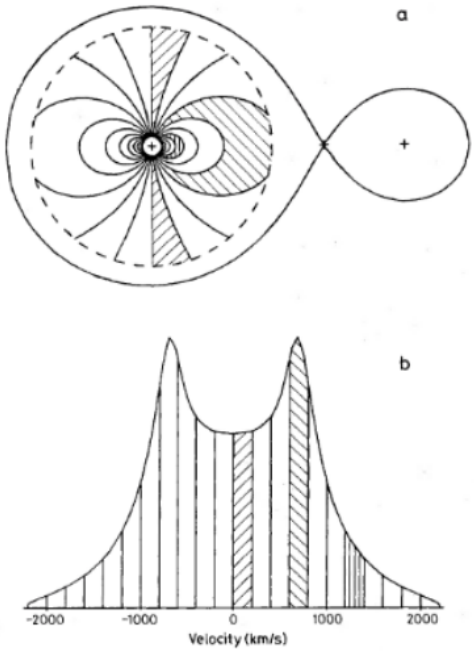

Figure 2.4: a) Fields of constant radial velocity in an accretion disk according to an observer b) Corresponding areas in an emission line (Marsh and Horne, 1988).

$$v_D = v_K \sin i \sin \phi, \tag{2.37}$$

where i is the disk inclination (face-on corresponds to 0° and edge-on to 90°) and phi is the azimuthal angle between a point on the disk and the projection of the line of sight onto the disk. Figure 2.4 illustrates the areas of constant radial velocities and the emission originating from those areas in a spectral line. If velocity of outer disk gas can be measured and the assumption of Keplerian velocities is valid, the radius can be calculated from

$$R_d = \frac{GM_1 \sin^2 i}{v_{out}^2} \tag{2.38}$$

Possibly the simplest method to estimate the velocities is measuring the peak-to-peak separation of the spectral lines. As the double-peaked structure

of the spectral lines originate from the rotation of the accretion disk, with the center of the peak corresponding to the edge of the disk, the velocity of the gas can be calculated from

$$v_K = \frac{\lambda_r - \lambda_l}{2\lambda_c} c \sin i \tag{2.39}$$

where λ_r, λ_l and λ_c are the wavelengths of the right peak, left peak and line center, respectively. The measured radius depends on the measured spectral line, as the emitted line depends on the local disk temperature. H_α is emitted in the cooler outer disk region, so it can be used to trace the disk edge. Similarly to eclipse mapping, the spectral lines can also be modelled and radius measured that way.

The peak-to-peak distance of the spectral line is expected to differ with the phase, as the the azimuthal variation of the outer disk is significant due to the gravitation of the secondary. However the variation should diminish when averaging over the period, so measurements can be made from averaged spectra. It should be noted again, that measuring the radius from gas velocities using Eq. 2.38 assumes that the velocities are circular and Keplerian. If that is not the case and the velocities deviate significantly, this assumption breaks down.

The aim of this thesis is to study the velocities of the outer accretion disk by comparing simulated disks with observational data. A good understanding of the outer disk kinematics is crucial in order to find reliable methods to measure the accretion disk size.

Chapter 3

Methods to study accretion disk kinematics

3.1 Doppler Tomography

Using time-resolved spectroscopy of CVs throughout their period, the velocity information can be extracted from the spectra into a two-dimensional velocity map, or a Doppler tomogram, developed by Marsh and Horne (1988). The Doppler map forms an inside-out image of an accretion disk. The faster-moving parts of inner disk are reflected on the outer edge of the velocity map, and vice-versa, the outer disk is reflected closer to the origin in the map. Figure 3.1 shows how different structures correlate in velocity and position coordinates; Figure 3.2 shows how the Doppler map is related to phase-resolved spectral lines.

The astronomical spectral data is often noisy and incomplete. Spectral data of CVs is often taken with about 5-10 minute exposures, and sometimes the observations have gaps in between. Thus, perfect inversion of spectral data to velocity maps is not possible. Maximum entropy method (MEM) was developed to cope with these kinds of problems. It compares a predicted data with observed one, and measures the goodness of the fit using χ^2 statistic. Several possible images are produced, and the one which is most uniform azimuthally while still fitting the data is picked.

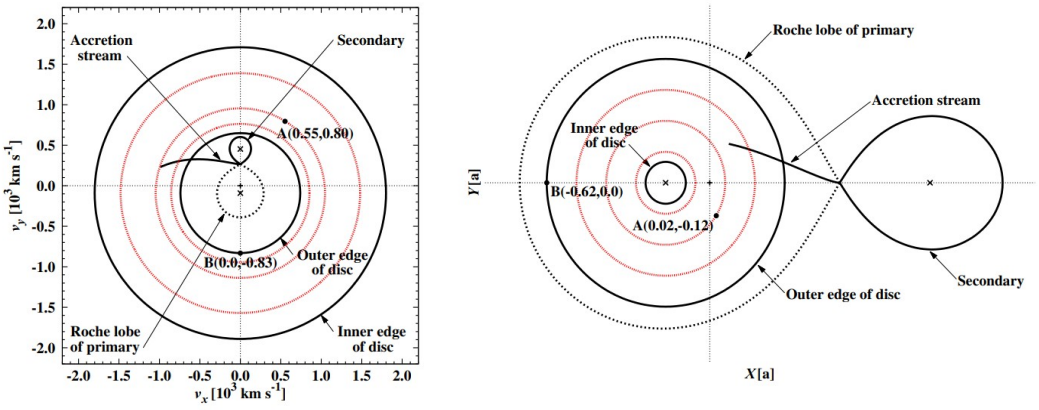

Figure 3.1: A schematic showing corresponding structures in velocity (left) and position (right) coordinates. The center of mass lies in origin, and locations of the primary and secondary stars are marked with a cross. Roche lobes of the primary and secondary are shown, as well as the 3:1 resonance radius (marked as outer edge of the disk) and inner radius at velocity 1800 km/s. The accretion stream leads from the secondary towards the disk (Kotze et al., 2015).

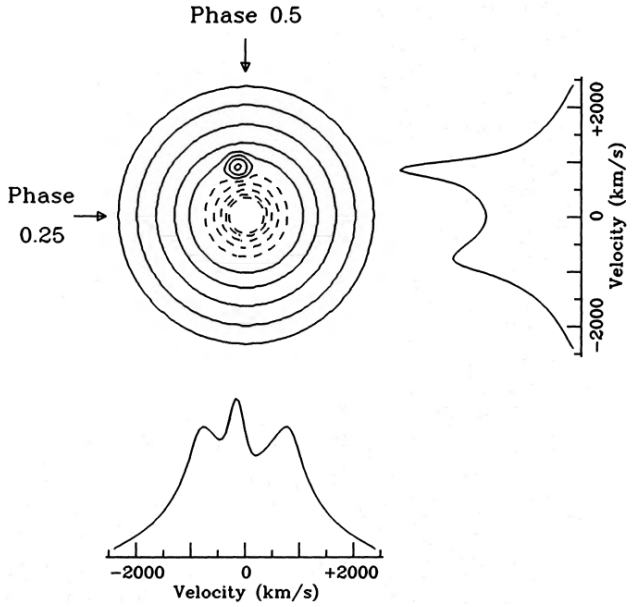

Figure 3.2: Spectral lines formed at phases 0.25 and 0.5, displaying their relation to a Doppler map (Marsh and Horne, 1988).

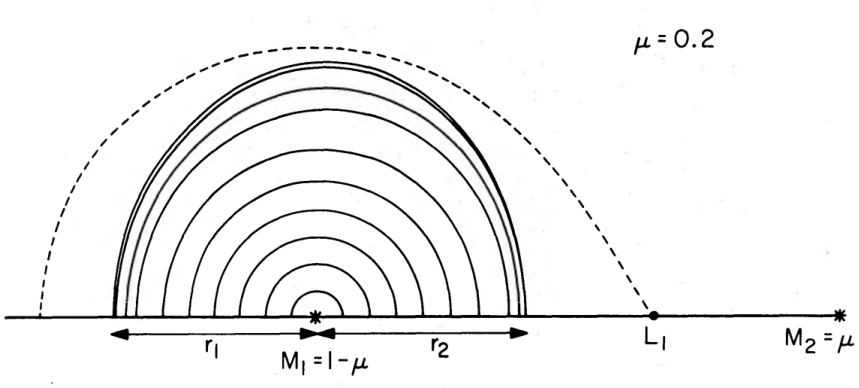

Figure 3.3: Streamlines of accretion disk are shown by solid lines. Dashed line represent the Roche lobe around primary, L_1 is the inner lagrangian point, r_1 is the maximum distance of the disk away from secondary and r_2 is the maximum distance of the disk towards secondary. μ is reduced mass, defined in Eq. 3.5 (Paczynski, 1977).

In this thesis, Fortran implementation by Spruit (1998) has been used to produce the Doppler maps, and slightly modified Python wrap by Hernandez Santisteban (2021) to plot the results.

3.2 Restricted three-body problem

Restricted three-body problem describes a situation where two massive objects orbit around a common center of mass and a third, light body moves in their gravitational field. This model is useful for simulating gas orbits in cataclysmic variables, as the mass of a gas atom is negligible compared to masses of the stars. The system is set up in co-rotating Cartesian coordinates, where the center of mass is at the origin and the x-axis is on the line connecting stars. The movement of the system is restricted to (x, y) plane, as the thickness of the disk is negligible compared to its extend on x and y directions. Thus, the primary and secondary stars lie at

$$x_1 = \frac{a}{1 + \frac{M_1}{M_2}} \tag{3.1}$$

$$x_2 = \frac{a}{1 + \frac{M_2}{M_1}}, \tag{3.2}$$

where a is the separation of the stars.

Trajectory of the particle is then governed by three forces: gravitational forces created by the stars, and Coriolis and centrifugal forces introduced by the co-rotating frame of reference. At this point, let's transfer to cylindrical coordinates for convenience. The derivatives are calculated with respect to angle instead of time, as it is more convenient to use in computational calculations. The equations of motions in r and ϕ directions are then

$$\begin{aligned}\frac{d^2r}{d\phi^2} =& \frac{r}{v_\phi}\Bigg(- G\frac{M_1}{r^2} - G\frac{M_2(r + a\cos\phi)}{(r^2 + 2ar\cos\phi + a^2)^{3/2}} \\ &+ r\Omega^2 + 2\Omega v_\phi + \frac{v_\phi^2}{r} + \frac{GM_2}{a^2}\cos\phi\Bigg)\end{aligned} \tag{3.3}$$

$$\frac{d^2\phi}{d\phi^2} = \frac{r}{v_\phi}\left(G\frac{M_2(a\sin\phi)}{(r^2 + 2ar\cos\phi + a^2)^{3/2}} - 2\Omega v_r - \frac{v_r v_\phi}{r} - \frac{GM_2}{a^2}\sin\phi\right) \tag{3.4}$$

where $\Omega = \frac{2\pi}{P}$ notates angular velocity of the binary and a is the binary separation.

We are interested in tracking particles in outer disk. Thus, we assume the particle to lie in the largest stable streamline. The streamlines have been calculated by Paczynski (1977) for a range of mass ratios. A linear regression model is fitted to numerical values of Paczynski, and the starting value of the distance from the primary (r_2, see Figure 3.3) is then calculated from the model for each system. Here

$$\mu = \frac{1}{\frac{M1}{M2} + 1} \tag{3.5}$$

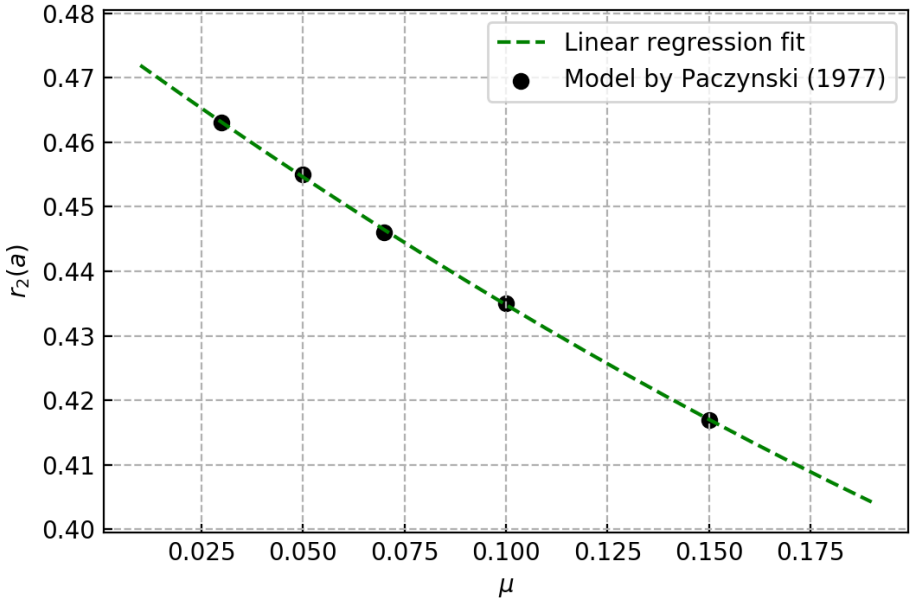

Figure 3.4: Largest stable streamline r_{max} as a function of μ. A linear regression model is fit to numerical values of Paczynski (1977)

.

is used for simplicity instead of mass ratio q.

After the initial position is found, the velocity of the particle is determined so that the orbit of the particle stays stable. The particle in the initial position should only have azimuthal velocity, as it lies at $\phi = 0$ between the primary and the secondary. After the particle has been initialized, the equations of motion 3.3 are integrated over angle ϕ using RK(4) integration.

3.3 Numerical integration using 4th order Runge-Kutta method

Runge-Kutta methods are a family of numerical solvers for first-order ordinary differential equations. In astronomy, probably the most used of these methods is the fourth order Runge-Kutta method, or RK(4). Let's describe the initial value problem as

$$\frac{dg}{dt} = f(g, t) \tag{3.6}$$

with an initial condition

$$g_0 = g(t_0). \tag{3.7}$$

In this thesis, both velocity and position of the particle in polar coordinates are integrated using RK(4). Thus, we have four initial value problems, as each of the aforementioned vectors have two dimensions. The initial conditions are

$$r(\phi = 0) = r_2 \tag{3.8}$$

$$v_r(\phi = 0) = 0 \tag{3.9}$$

$$v_\phi(\phi = 0) = v_\phi \tag{3.10}$$

Here r_2 is the maximum distance of the outermost stable orbit in the direction of the secondary (see Figure 3.3), and v_ϕ is some arbitrary initial velocity. The next step taken during an angle change $d\phi$ is then always calculated

from

$$g_{n+1} = g_n + \frac{1}{6}(k_1 + 2k_2 + 2k_3 + k4) \tag{3.11}$$

where

$$k_1 = dtf(\phi_n, g_n) \tag{3.12}$$
$$k_2 = dtf\left(\phi_n + \frac{1}{2}d\phi, g_n + \frac{k_1}{2})\right) \tag{3.13}$$
$$k_3 = dtf\left(\phi_n + \frac{1}{2}d\phi, g_n + \frac{k_2}{2})\right) \tag{3.14}$$
$$k_4 = dtf(\phi_n + d\phi, g_n + k_3) \tag{3.15}$$
$$\tag{3.16}$$

In our case, we know that

$$\frac{dr_n}{d\phi} = v_{rn}\frac{r}{v_\phi} \tag{3.17}$$
$$\frac{dv_{rn}}{d\phi} = a_{rn}\frac{r}{v_\phi} \tag{3.18}$$
$$\frac{dv_{\phi n}}{d\phi} = a_{\phi n}\frac{r}{v_\phi} \tag{3.19}$$
$$\tag{3.20}$$

Thus, some formulating of equations of motion to find the acceleration of a particle in position (r, ϕ) is needed.

3.4 Smoothed Particle Hydrodynamics

Smoothed particle hydrodynamics (SPH) is a numerical method for solving hydrodynamical situations. The system is modelled with a set of particles, which have properties of the material (such as density, temperature, velocities), and which move according to conservation laws. Originally it was developed to simulate non-axisymmetrical problems in astrophysics (Gin-

gold and Monaghan, 1977), but later it has been used for a wide variety of situations in both astronomy and other sciences. The detailed description of the method is beyond the scope of this thesis, and only the most important things are discussed here. For a comprehensive review, please see Liu and Liu (2003).

3.4.1 Smoothing function

Interpolation of any function $f(r')$ will be calculated with the help of a smoothing function:

$$\langle f(r)\rangle = \int dr' f(r') W(r, r', h) \tag{3.21}$$

Here r' is the position of a particle, r is the position where $f(r')$ will be interpolated to, h is smoothing length and W is the interpolating kernel. A smoothing function is the key property of SPH. It defines the so-called support domain for a particle, or in other words, the area the particle has effect on. The smoothing function (also spoken of as *kernel*) used in modelling accretion disks is a spherically symmetrical W_4 spline normalized to two dimensions (Monaghan and Lattanzio, 1985):

$$W_4(r,h) = \begin{cases} \frac{40}{7h^2\pi}(1 - 6q^2 + 6q^3), & q < \frac{1}{2} \\ \frac{80}{7h^2\pi}(1-q)^2, & \frac{1}{2} \leq q < 1 \\ 0, & q \geq 1 \end{cases} \tag{3.22}$$

where $q = r/h$ and h is *smoothing lenght*. The smoothing length is a number describing the extent of the support domain. It need not necessarily be a constant, as it can vary from place to place. However, in the SPH simulations of accretion disks within the range of this thesis, it is a constant number.

3.4.2 Viscosity in SPH

Artificial viscosity is implemented in hydrodynamical simulations to deny two particle streams to pass through each other. This is done by making approaching particles repel each other with forces depending on the particle velocities. This artificial viscosity is not to be mistaken with the fluid viscosity discussed earlier, but is used simply to forbid nonphysical situations. In accretion disk simulations implementing artificial viscosity causes problems, as the different disk annuli in a differentially rotating disk repel each other and cause slowing down with too high magnitudes. Thus, accretion disk simulations are done with very low or no artificial viscosity, except in shock situations (in hot spot area, for example). The version of SPH accretion disk simulations in this thesis uses artificial viscosity described by Monaghan and Gingold (1983). It was developed to produce required dissipation - conversion of kinetic energy to thermal energy - at shock fronts. The formulation for this is

$$\Pi_{ij} = \begin{cases} \dfrac{-\alpha_\Pi \bar{c}_{ij}\phi_{ij} + \beta_\Pi \phi_{ij}^2}{\bar{\rho}_{ij}} & , \quad v_{ij} \cdot x_{ij} < 0 \\ 0 & , \quad v_{ij} \cdot x_{ij} \geq 0 \end{cases} \tag{3.23}$$

where

$$\phi_{ij} = \frac{h_{ij} v_{ij} \cdot x_{ij}}{|x_{ij}|^2 + \varphi^2} \tag{3.24}$$

$$c_{ij} = \frac{1}{2}(c_i + c_j) \tag{3.25}$$

$$\bar{\rho_{ij}} = \frac{1}{2}(\rho_i + \rho_j) \tag{3.26}$$

$$h_{ij} = \frac{1}{2}(h_i + h_j) \tag{3.27}$$

$$v_{ij} = v_i - v_j, \; x_{ij} = x_i + x_j \tag{3.28}$$

x_{ij} here is the vector from the shock front to the particle and v_{ij} is its velocity vector. The parameter α_Π describes shear viscosity and β_Π bulk viscosity.

$\varphi = 0.1h_{ij}$ is added to prevent numerical divergence when two particles come close to each other. c_{ij} and ρ_{ij} have their typical meanings of sound speed and density, respectively. The artificial viscosity Π constructed this way is added then into pressure terms of the SPH simulations.

β is generally set to zero in accretion disk simulations, but α often has a value. Setting it properly can be a bit tricky though, as correct shock treatment would require $\alpha \sim 1$, but that large a value causes too large shear viscosity (Monaghan, 1992). Thus, α needs to be adjusted to the situation; if one is interested in the shock areas, a larger value should be used, but if one is more interested in areas without remarkable shock fronts, such as the outer realms of the disk discussed in this thesis, it can be mostly ignored or set to a small value.

3.4.3 Simulating accretion disks with SPH

The hydrodynamical processes in the disk can be described with *Navier-Stokes equation*. In the case of accretion disks, the equation can be formulated as e.g. Flebbe et al. (1994), Landau and Lifshitz (1987)

$$\begin{aligned}\frac{dv}{dt} =& -\frac{\nabla P}{\rho} + \frac{1}{\rho}\sigma_{ab} - G\left(\frac{M_1(r-r_1)}{(r-r_1)^3} + \frac{M_2(r-r_2)}{(r-r_2)^3}\right) \\ & - 2(\Omega \times v) + \Omega^2(r - r_{CM})\end{aligned} \tag{3.29}$$

Here σ_{ab} denotes a viscous stress tensor and r_{CM} refers to the location of the center of mass.

$$\sigma_{ab} = \eta\left(\frac{\partial v_a}{\partial r_b} + \frac{\partial v_b}{\partial r_a} - \frac{2}{3}\delta_{ab}\frac{\partial v_c}{\partial r_c}\right) + \zeta\delta_{ik}\left(\frac{\partial v_c}{\partial r_c}\right)^2 \tag{3.30}$$

The viscous stress tensor describes the changes from both *dynamic viscosity* η and so-called *second viscosity*, or *bulk viscosity* ζ. Both must be positive coefficients independent of velocity. In the case of outer parts of accretion disks, the bulk viscosity is not relevant and set to zero. The dynamic viscosity

is related to the kinetic viscosity η , only scaled with density:

$$\nu = \rho\eta \tag{3.31}$$

Thus, the Navier-Stokes equation used in SPH simulations in this thesis is reduced to form

$$\begin{aligned}\frac{dv}{dt} = &-\frac{\nabla P}{\rho} + \nu\left(\frac{\partial v_a}{\partial r_b} + \frac{\partial v_b}{\partial r_a} - \frac{2}{3}\delta_{ab}\frac{\partial v_c}{\partial r_c}\right) - \\ &G\left(\frac{M_1(r-r_1)}{(r-r_1)^3} + \frac{M_2(r-r_2)}{(r-r_2)^3}\right) - 2(\Omega \times v) + \Omega^2(r - r_{CM})\end{aligned} \tag{3.32}$$

The gas in accretion disks is close to ideal gas. Thus, the gas pressure can be calculated from

$$P = k_B \rho T, \tag{3.33}$$

where k_B is the Boltzmann constant. As the gas interacts in a viscous manner, it is only natural that some of the kinetic energy is transferred into heat, thus increasing the entropy in the system. This energy dissipation per unit mass can be calculated from Landau and Lifshitz (1987):

$$T\frac{dS}{dt} = \frac{\eta}{2\rho}\sigma_{ab}\sigma_{ab}, \tag{3.34}$$

SPH Simulation code for accretion disks was kindly provided by the supervisor of this thesis, and it is based on Liu and Liu (2003). The disk simulations were done in two dimensions. The simulations were started with an empty disk, when the secondary just starts to lose mass. Because we were not interested in the disk formation process, the initial mass transfer rate was set unrealistically high until the disk spread out and stabilized. Then the mass transfer rate was set to more realistic numbers, about $10^{-18} M_\odot/\mathrm{s}$, and the simulation was ran again until some sort of equilibrium state.

The time integration is done using Cash-Karp method. Cash-Karp method is a numerical method for solving ordinary differential equations that belongs to a family of Runge-Kutta solvers (Cash and Karp, 1990). It calculates

fourth and fifth order solutions to the ordinary differential equation, and then compares them. The difference between these solutions is taken as the error in the fourth order estimate. Thus, it's possible to make the solver adaptable; as long as the error stays reasonable, a larger time step can be used, but if the error becomes too large the time step can be adjusted to smaller value.

The simulated disks are not stationary, but precess around the white dwarf. In order to make it possible to compare the simulations to observed Doppler tomograms, simulation results were binned to (300pix x 300pix) 2D histograms and a median over 10 orbits was taken. The result is thus a compiled image over several orbits, and should not be mistaken to an image of a disk at some arbitrary time step.

3.5 A note on trailed spectra

Trailed spectra presented in next chapter have been reconstructed from the velocity map produced by SPH simulations and Doppler map constructed from time series of spectra. Reconstruction in both cases was done by flattening binned 2d histograms with respect to x- axis to form 1d histogram. The original 2d histogram was then rotated $2\pi/100$ radians and flattened again. Process was repeated until a single rotation was done, essentially creating 100 time-resolved reconstructed spectra. Individual spectra were then presented as heat map slices along x-axis, piled according to phase along y-axis.

While this is the only realistic way of seeing what spectral lines from simulated situation could look like, the method comes with some fall-backs when used instead of raw observational spectra. Some spectral features are lost when reconstructing spectra from Doppler map. When building a Doppler map from individual spectra, it is assumed that all points are visible all the time. Thus, when anisotropies occur in the system, they might be lost in the spectra to Doppler map to spectra transition. Reconstructed spectrum will be more blurred than the original one due to the binning processes in the map construction and possible interpolation used in displays. Finally, some

artefacts may be added to the reconstructed spectra. It is not uncommon for the Doppler maps to have artificial lines passing through the image that do not represent any real feature in the system. These are naturally added to the reconstructed spectra.

Thus, analysing reconstructed trails should not be done without comparing them to raw spectra, as is usually done. In this thesis this step is however skipped, as we're only interested in the bright disk area, and especially the outer disk edge, that does not suffer too much from the aforementioned fallbacks.

Chapter 4

A selection of CVs

Table 4.1: Used system parameters for the selected Cataclysmic variables

System	$M_1/M_\odot$	q	P_{orb}/d	i/deg	K_1/km/s	γ/km/s	cite
HT Cas	0.61	0.15	0.074	81	58	-9	[a]
U Gem	1.2	0.35	0.177	69.7	107	42	[b]
WZ Sge	0.85	0.09	0.057	77	47.1	-72	[c]
BW Scl	0.92	0.059	0.054	63.4	27.7	-17.5	[d]

[a] Horne et al. (1991)
[b] Echevarría et al. (2007)
[c] Steeghs et al. (2007)
[d] Neustroev and Mäntynen (2022)

Four systems were selected for analysis of gas velocities in the outer disk. BW Sculptoris and WZ Saggitae represent low mass ratio ($q = 0.059$ and $q = 0.09$, respectively) systems with short orbital period. Due to close proximity of the secondary star, they have non-axisymmetric disks extending beyond last non-intersecting orbit. For comparison, HT Cassiopeia and U Geminorum were selected to represent systems with higher mass ratios ($q = 0.15$ and $q = 0.35$) and longer periods. System parameters are gathered in Table 4.1.

All systems are presented with observational Doppler map of the H_α line, and velocity and position maps received from SPH simulations. Additionally, trailed spectrum was reconstructed from both observational Doppler map and the simulated velocity map. The H_α line was chosen for this study for two

reasons: it is usually the most prominent feature in CV spectra, and it is thought to trace well the outer disk areas due to relatively lower emission temperatures compared to other Balmer lines or helium lines.

4.1 U Gem

U Gem is the first discovered cataclysmic variable and the archetype of U Gem type dwarf novae (Hind, 1856). It has a long orbital period of over 4 hours and recurrent outbursts with average interval of 118 days, brightening by about 5 magnitudes and lasting roughly 12 days (Szkody and Mattei, 1984). Its light curve shows eclipses of the disk, but the white dwarf is visible at all times. Superhumps have been observed in U Gem during a superoutburst (Smak and Waagen, 2004), which is highly unexpected as the superhumps are though to be caused by the accretion disk expanding beyond 3:1 resonance radius, causing the disk to become elliptic and start precessing. Disks this large are expected to be found in systems with shorter orbital periods, mainly in WZ Sge-type dwarf novae (see Chapter 4.3). Spectroscopically U Gem is a very typical dwarf nova with bright, double-peaked Balmer and helium lines.

U Gem was observed in quiescence on 2007 September 9 using UVES the Ultraviolet and Visual Échelle Spectrograph (Dekker et al., 2000) mounted on the ESO Very Large Telescope (VLT) at the Paranal Observatory in Chile. The incoming light is split into two arms, blue and red, with accessible wavelengths 3000Å-5000Å and 4200Å-11 000Å, respectively. The data set used here, taken with the red arm, consists of 97 individual spectra with 80 second exposure time covering only 0.7 orbital periods. Wavelength calibration was done using ThAr lamps. The data was reduced using EsoReflex pipelines provided by ESO.

The H_α Doppler map (Fig. 4.1) shows a symmetric, featureless and egg-shaped accretion disk. The outer disk velocities seem to agree well with last non-intersecting orbit overplotted in the Doppler map. A bright spot slightly ahead of the secondary star can be seen, not to be mistaken with the secondary star. It has been noted that it could originate either from

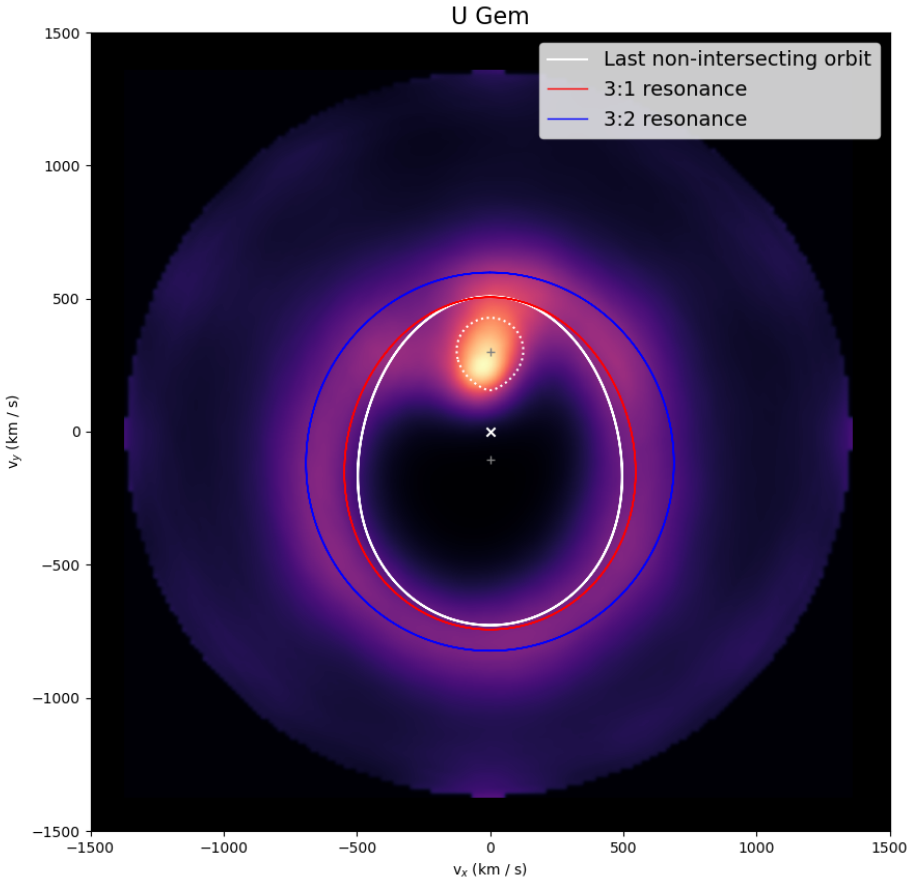

Figure 4.1: H_α Doppler map of U Gem in quiescence. Star locations are marked with grey '+' and center of mass is marked with white 'x'. Selected resonance orbits and last non-intersecting orbit are overplotted together with the Roche lobe of the secondary star

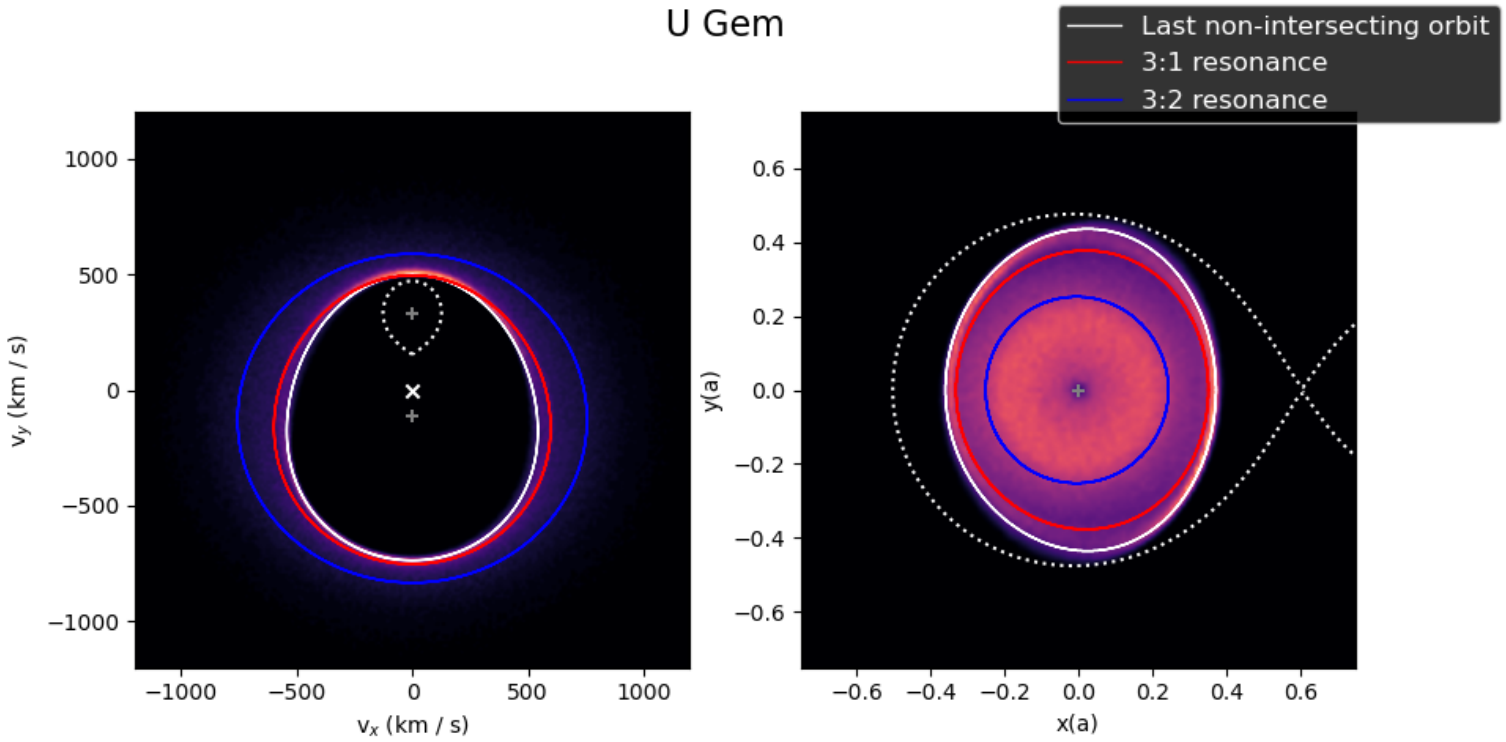

Figure 4.2: SPH simulation results for U Gem, projected to velocity coordinates in the left image and position coordinates in the right image. Primary and secondary stars are marked with grey '+', and center of mass with white 'x'. Roche lobes of primary (in right-hand image) and secondary (in left-hand image) are overplotted, together with selected resonance orbits and last non-intersecting orbit.

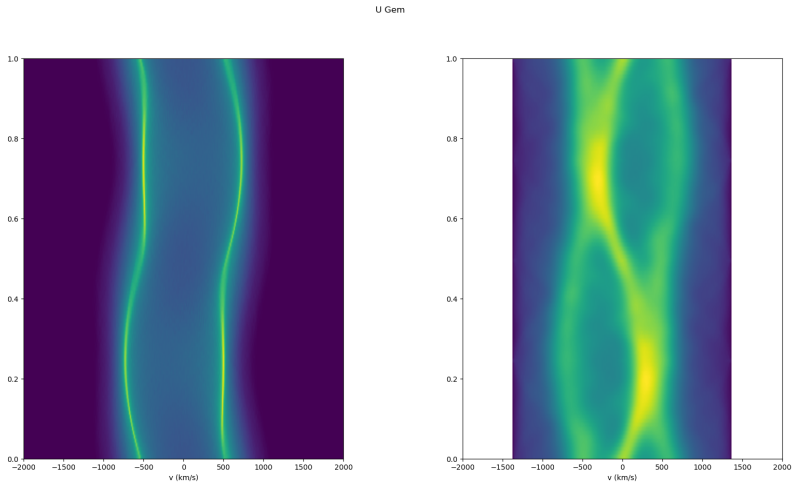

Figure 4.3: Reconstructed trailed spectrum of U Gem, SPH simulated velocity map on the left image and observed data on the right.

the surface of the secondary or at a shock front with the accretion disk (Echevarría et al., 2007).

Likewise, the simulated velocity map (Fig. 4.2, left) shows quite a blank and featureless accretion disk with very even particle distribution. The only denser areas are located on the top and bottom sides of the disk in velocity map. No spiral arms are found. The position map (Fig. 4.2, right) shows an even disk extending up to, and slightly beyond, the last non-intersecting orbit. This aligns with the observations of superhumps in U Gem. The inner disk inside 3:2 resonance radius is more populated than the disk outside. Two elongated, dense areas are however found between 3:1 resonance radius and last non-intersecting orbit: one on the side next to the secondary side, and one opposite to it.

The reconstructed trail of observed spectra can be found on right-hand side in Figure 4.3. It shows a clear trail from the bright spot ahead of secondary star, together with spectral line peaks. The peak trails themselves show waves curving in opposite directions from the bright spot trail, and are caused by the elongated shape of the accretion disk. Exactly the same waves are seen in the reconstructed trail from simulated velocity map, on left-hand side of Figure 4.3. The more populated areas of the velocity map can be seen

here as enhanced brightness on the trails around phases 0.2 and 0.8.

4.2 HT Cassiopeia

HT Cas is a SU Uma type star discovered by Hoffmeister (1943). It has orbital period of 1.77h (Patterson, 1981) and a mass ratio of 0.15 (Horne et al., 1991). Its brightness varies between 13.0-16.5 magnitudes, with quiescent light variations between about 16 to 18 magnitudes. The light curve studies (e.g., Patterson, 1981; Wood et al., 1995) show deep eclipses of the primary, but accretion disk component is very dim. HT Cas exhibits visible superhumps in outburst (Zhang et al., 1986). Spectroscopically HT Cas shows typical high-inclination CV behaviour, with clearly double-peaked Balmer lines as the most prominent feature.

The observations were done on 2005 October 29 and 31, using 2.1 m telescope at Observatorio Astronomico Nacional in Mexico. The telescope was equipped with Boller & Chivens spectrograph, covering wavelengths 4600-6700 Å (first night) and 6150-7225 Å (second night) with a dispersion of 1.05 Å / pixel. 40 spectra of 293 seconds in exposure time were taken each night.

Doppler map presented in Figure 4.4 was provided by Dr. Vitaly Neustroev. Its most prominent features are a bright, extended emission feature on the second quadrant of the disk and the hot spot on the fourth quadrant. An emissive structure, possibly from spiral arm origin, can be found around the hot spot, extending symmetrically to both trailing and leading side. Plenty of disk material is found outside the last non-intersecting orbit, suggesting a large accretion disk.

In simulated velocity map (Fig. 4.5) two particle dense areas due to spiral arms can be seen: one in third quadrant extending towards negative v_y axis from hot spot area, and another extending all throughout the opposite side.

The position map shows a large disk extending up to the last non-intersecting orbit. Slight overflow is observed on the first quadrant and on the side opposite to the secondary star. Two spiral arms can be seen on top and bottom of the disk, extending outwards from the dense inner disk inside 3:2 resonance radius.

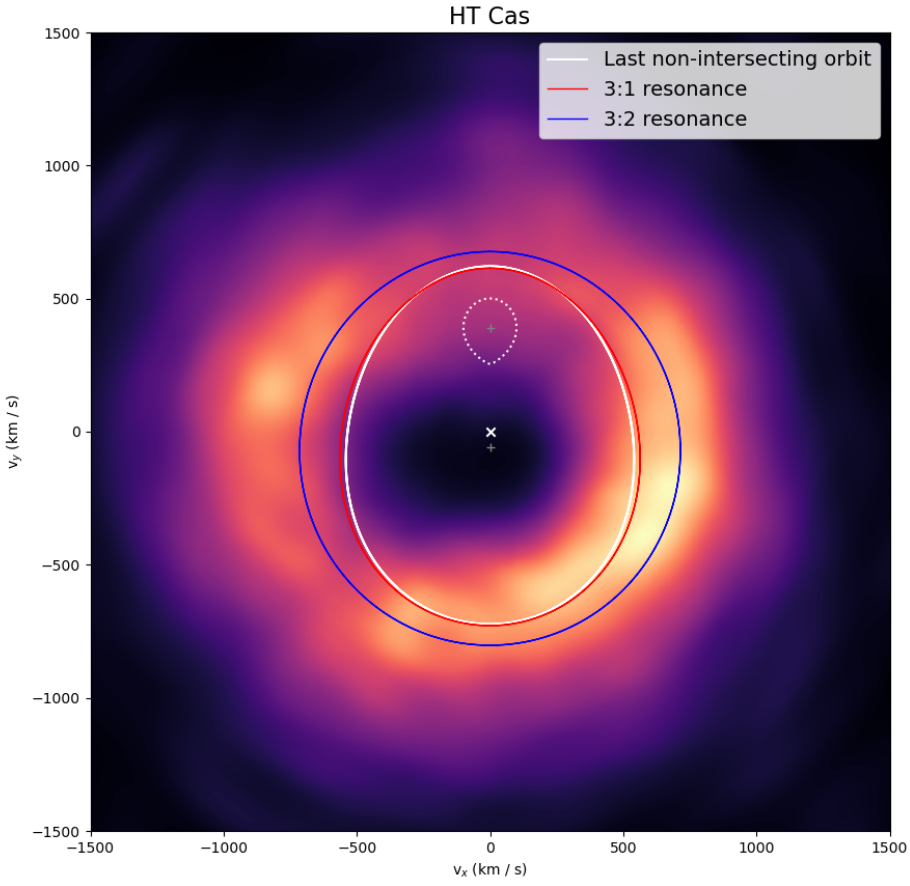

Figure 4.4: H_α Doppler map of HT Cas in quiescence. Star locations are marked with grey '+' and center of mass is marked with white 'x'. Selected resonance orbits and last non-intersecting orbit are overplotted together with the Roche lobe of the secondary star.

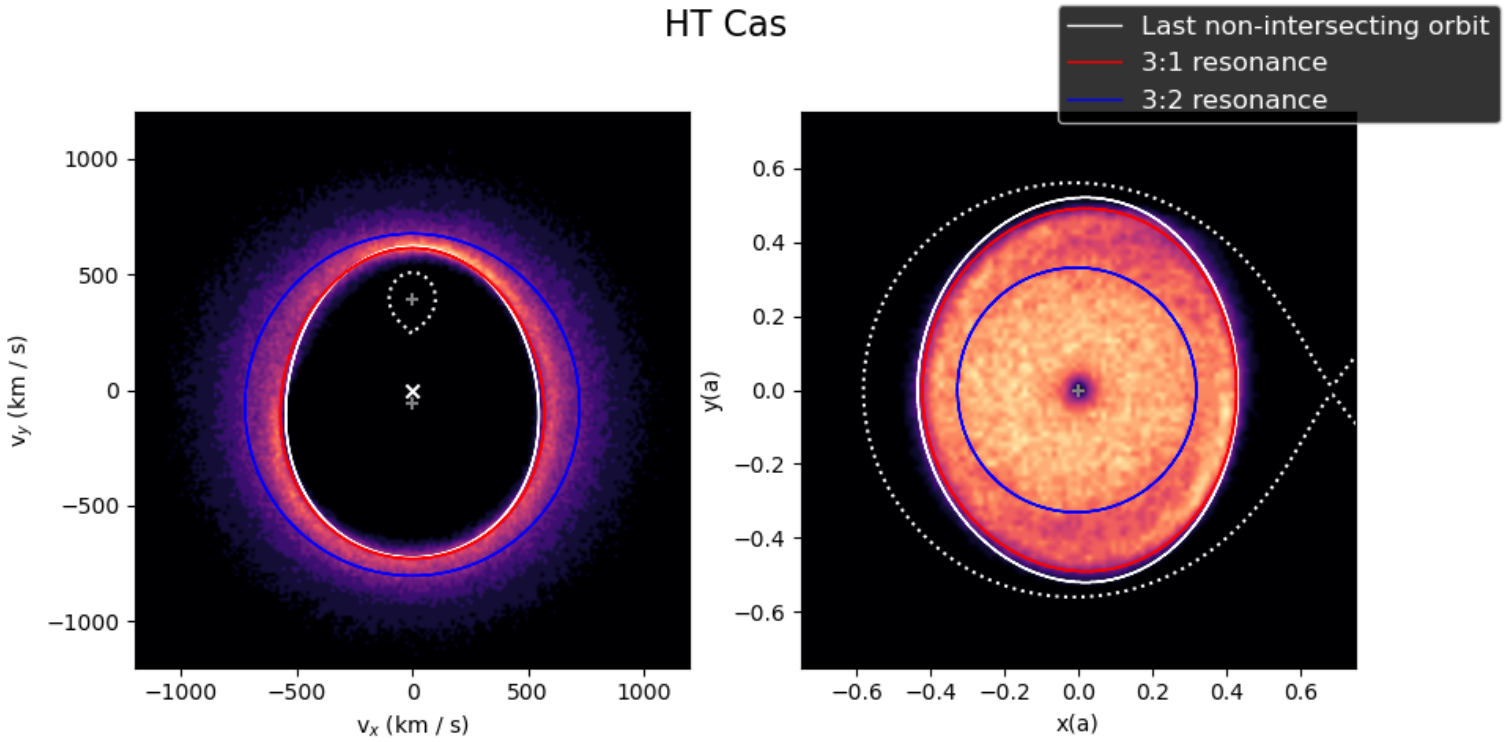

Figure 4.5: Accretion disk images of HT Cas resulting from SPH simulations. Left side shows the disk in velocity space, and right side in position coordinates. Primary and secondary stars are marked with grey '+', and center of mass with white 'x'. Roche lobes of primary (in right-hand image) and secondary (in left-hand image) are overplotted, together with selected resonance orbits and last non-intersecting orbit.

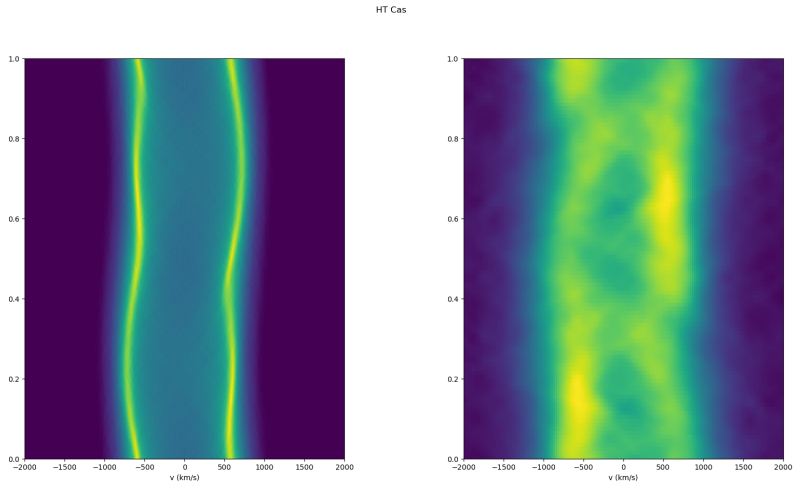

Figure 4.6: Reconstructed trailed spectrum of HT Cas, with SPH simulated velocity map on the left image and observed data on the right.

The reconstructed trailed spectrum from observations (Fig. 4.6, right) shows the S-wave of hot spot. On the opposite phases, on left peak between phases 0.0-0.2 and 0.4-0.8 one can see strong emission from the extended area of enhanced emission clearly seen also in Doppler map in Figure 4.4.

Trail reconstructed from simulated velocity map shows two clear peaks with no features in the middle of them. The peak trails shift with phase. Here the elongated shape of the outer disk in velocity space can be clearly seen: The bottom of the disk leaves a broad hump between phases 0.0-0.5 on left side and 0.4-1.0 on right side, while the top of the disk trails a narrower mark between phases 0.5-0.9 on left side and 0.1-0.4 on right side.

4.3 WZ Sagittae

WZ Sge is one of the oldest known and most popular cataclysmic variable: it was already listed in the Catalogue of Variable Stars found from Harvard plates (Cannon, 1907). It is the archetype of WZ Sge-type dwarf novae, characterised with bright outbursts with slow declines and long intervals between outbursts. In this type of systems, orbital period deviations known

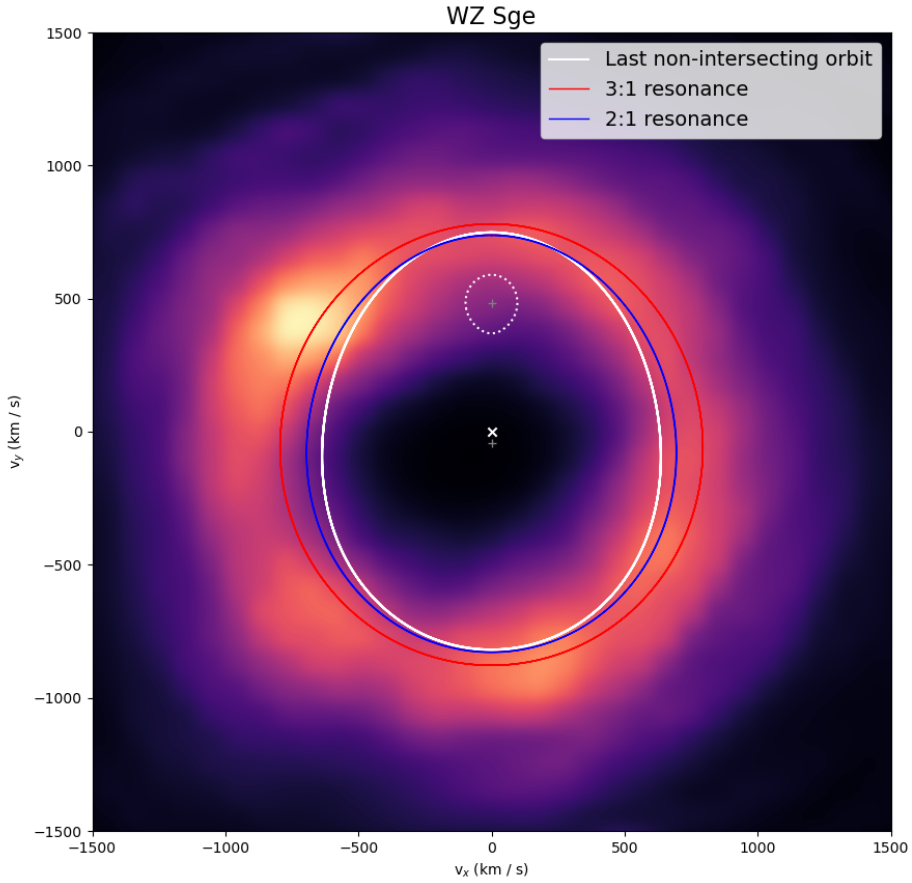

Figure 4.7: H_α Doppler map of WZ Sge in quiescence. The Doppler map shows a symmetrical gas disk with a hot spot in the fourth quadrant. Low-emission areas are found trailing and leading the hot spot. Positions of stars are marked with grey '+' and center of mass is marked with white 'x'.

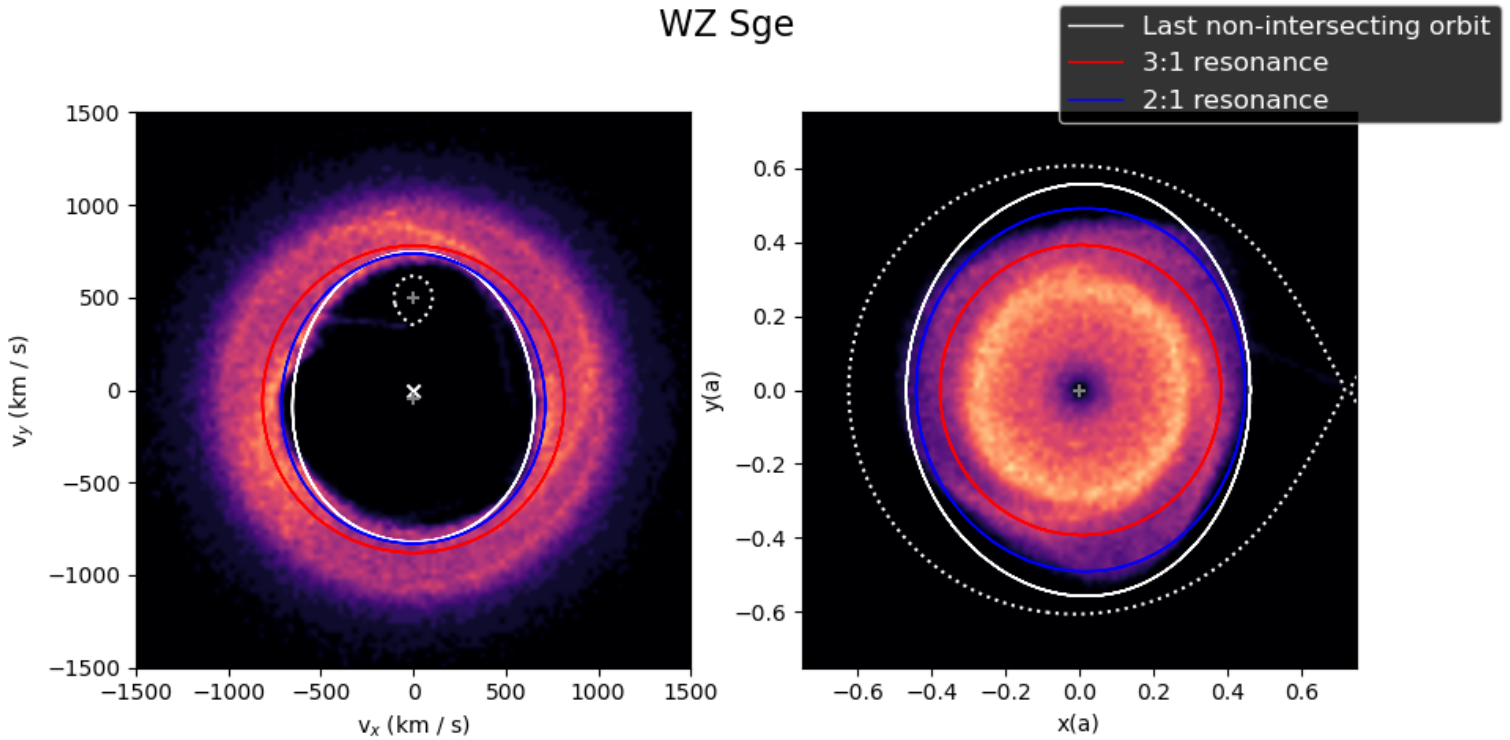

Figure 4.8: SPH simulation results of WZ Sge projected to velocity (left) and position (right) coordinates. Most prominent features here are the bulge in velocity map, dense inner ring in position map, and spiral arms found in both maps. Positions of stars are marked with grey '+' and center of mass is marked with white 'x'. Roche lobes of the primary (in position map) and secondary (in velocity map) are overplotted, together with selected 3-body orbits.

as superhumps are observed. WZ Sge is fairly evolved system, with orbital period of 82 minutes and small mass ratio of 0.09 (Steeghs et al., 2007).

WZ Sge was observed with 2.5m Isaac Newton telescope equipped with a medium to low resolution, long-slit spectrograph, the Intermediate Dispersion Spectrograph (IDS), on 1995 July 21-23. The data set, covering wavelengths 5800-7100Å, consists of 55 individual spectra with 200 sec exposure time and a spectral resolution of 2Å. The observations covered in total over 9 orbital periods. Comparison spectra, taken with CuAr lamp, were taken throughout the observations and used for wavelength calibration. Data reduction was performed using **iraf** environment.

The Doppler map in H_α (Fig. 4.7) shows an azimuthally semi-symmetric disk with a clearly visible hot spot. A lack of emission is spotted tracking the hot spot, and the leading side shows a slight bulge extending towards $-v_x$. The quality of the spectra is poorer with INT IDS than with X-SHOOTER - thus, the resulting map is blurrier and shows quite a lot of emissive material beyond the last non-intersecting orbit. However, it is clear that the accretion disk extends up to the last non-intersecting orbit and possibly even beyond.

Median velocity and position maps resulting from SPH simulations for WZ Sge can be found from Figure 4.8, with velocity map on the left and position map on the right. WZ Sge shows a bulge extending towards negative x-velocities leading the area where hot spot would be. Particles beyond the last non-intersecting orbit are found trailing and leading the bulge. Spiral arms can be seen on the upper area of the projected disk, as well as on the left- and right-hand sides.

The position map shows upside-down triangular shape of the outer accretion disk with a dense ring around the center of the disk at circularization radius. Three spiral arms extend from the ring towards outer disk. The disk extends close up to and beyond the last non-intersecting orbit at the tips of the triangle, but stay well inside 2:1 resonance orbit elsewhere.

Trailed spectrum reconstructed from observational data is shown on right side of Fig. 4.9. It shows a clear S-wave from the hot spot transferring from left to right peak of the spectral line. Additional trail travelling between peaks can also be found, corresponding to area of enhanced emission roughly

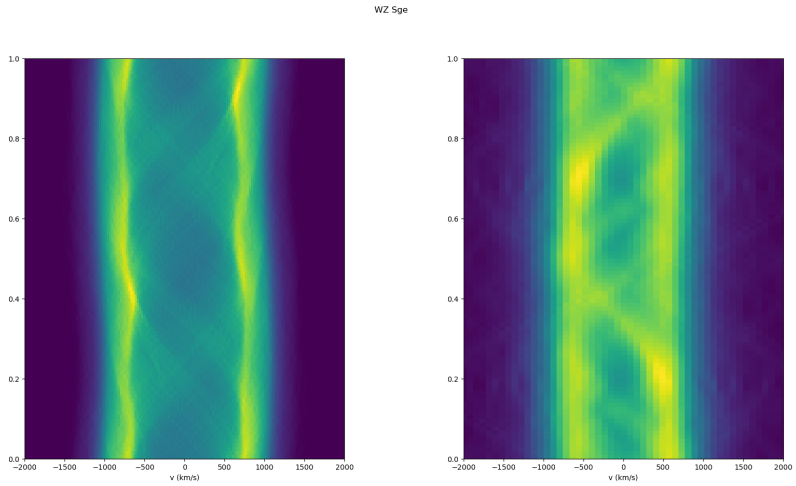

Figure 4.9: Reconstructed trailed spectrum of WZ Sge from SPH simulated velocity map (left) and observed data (right).

0.3 phases ahead of the hot spot, or bottom area of the disk in Doppler tomogram.

Reconstructed trailed spectra from SPH simulation is shown on left-hand side of Fig. 4.9. It shows clear trails of the spectral line peaks, wobbling due to non-round projected shape of outer disk. A shadow caused by the bulge can be seen travelling from right to left between phases 0.1 and 0.4, and back to right between phases 0.6 and 0.9. On opposite phase, the slight trail from particles laying between the first and second quadrants of the velocity map can be found.

4.4 BW Sculptoris

BW Scl is a WZ Sge-type dwarf nova, found in 1997 as a bright source in UV by Hamburg/ESO quasar survey and a bright X-ray source in ROSAT survey (Augusteijn and Wisotzki, 1997). Its orbital period of only 78 minutes is one of the shortest known yet.

Doppler map of H_α line (Figure 4.10) was kindly provided by Iikka Mäntynen. Its most prominent features are a gas ring with a gap in upper part

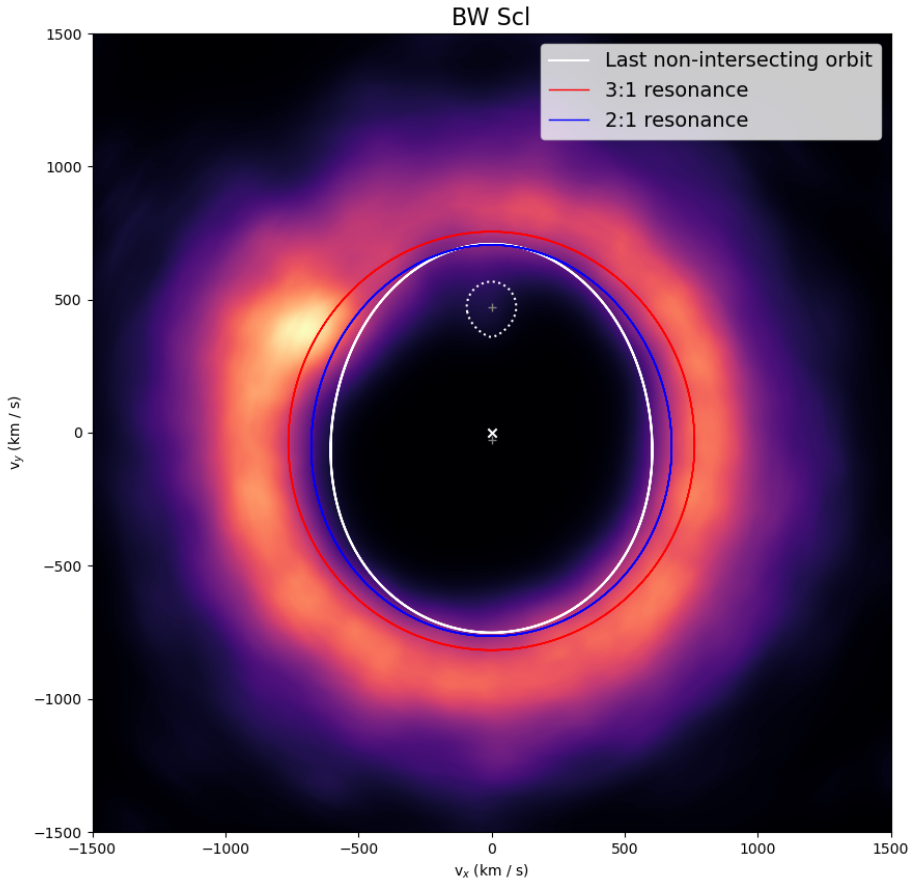

Figure 4.10: H_α Doppler map of BW Sculptoris. A gas disk with clearly visible hot spot in fourth quadrant can be seen. Selected resonance orbits and last non-intersecting orbit are overplotted.

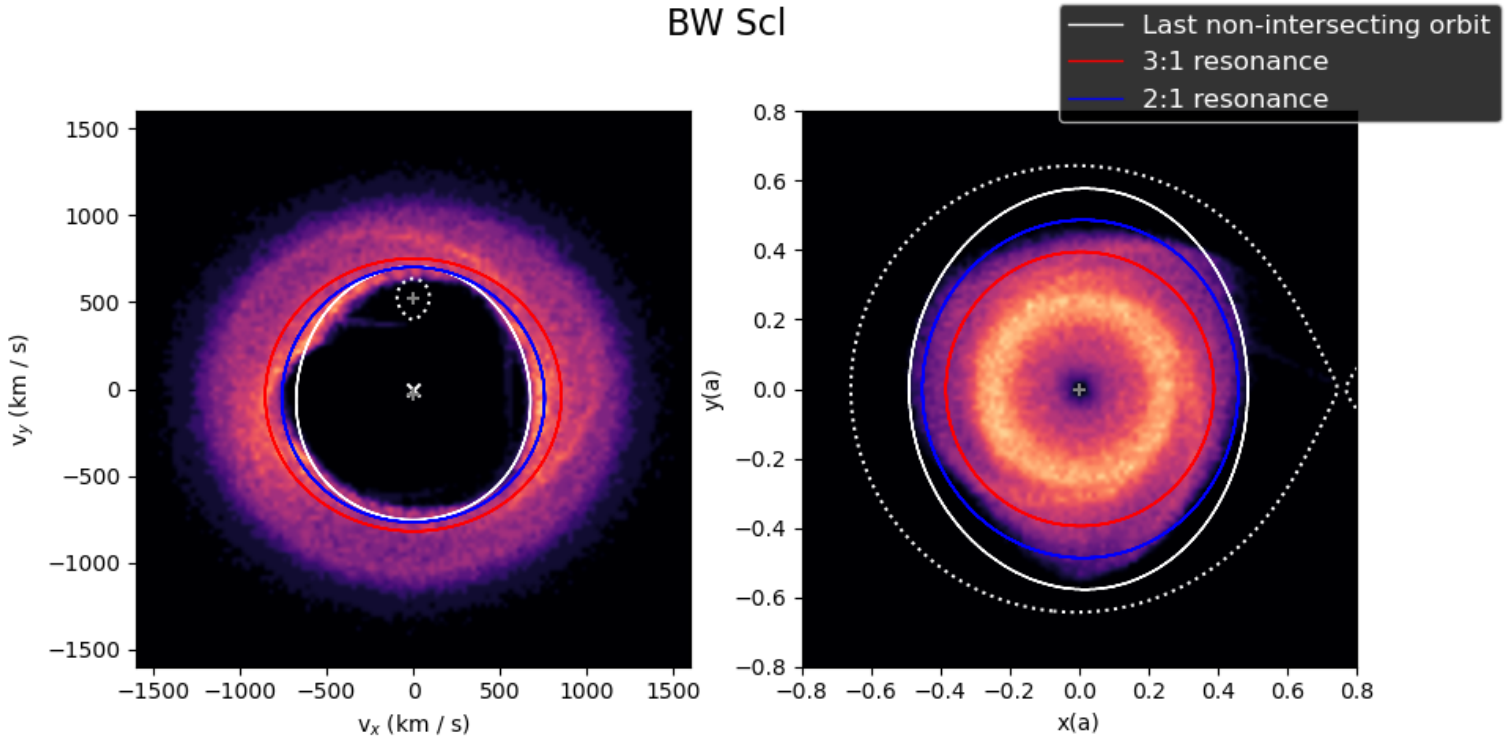

Figure 4.11: Simulated velocity map (left) and corresponding position map (right) of BW Scl. Positions of stars are marked with grey '+' and center of mass is marked with white 'x'. Roche lobes of the primary (in position map) and secondary (in velocity map) are overplotted, together with selected 3-body orbits.

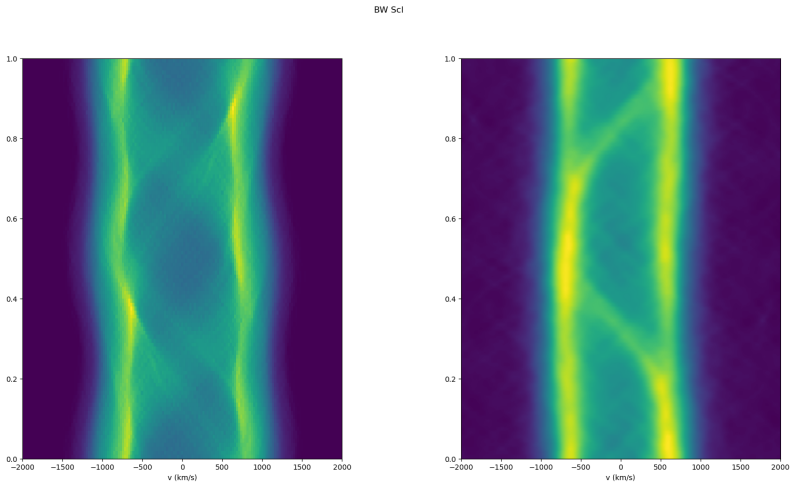

Figure 4.12: Reconstructed trailed spectrum of SPH simulated velocity map (left) and observed data (right).

and a visible hot spot in 4th quadrant. Secondary star is barely visible here. Gas extends well past 3:1 and even 2:1 resonance orbits, up to the last non-intersecting streamline.

SPH simulation results for BW Scl can be found in Figure 4.11. The velocity map shows a disk with a noticeable bulge towards inner disk, or $-v_x$, right after where the accretion stream hits the accretion disk. Overflow of particles beyond last non-intersecting orbit is found in third and fourth quadrants, on both sides of the bulge. Three spiral arms are seen, one on top side and two on left and right side of the disk.

The position map shows asymmetrical disk with a clear, dense ring close to 3:2 resonance orbit. The outer disk has an upside-down triangular shape due to the close proximity of the secondary star and its gravitational effects on the disk. The absence of the particles on top part of the disk can be seen as the bulge on the velocity map, with the slight particle overflow visible close to the accretion stream.

Reconstructed trailed spectrum from observed data is shown in Fig 4.12 right side, and reconstructed trailed spectrum from the velocity map based on SPH simulations is shown in left side. Trailed spectrum from observed data shows S-wave originating from the hot spot moving between left and

right peaks of the spectral line. A gap can be seen on right peak between phases 0.2 and 0.4, and at left peak at phases 0.7-0.9.

Compared, the trailed spectrum from simulated velocity map shows quite different features. Outer disk edge shows clearly on both left and right peaks, similarly to the trail of observed spectra. However, here velocity deviations originating from the egg-shaped outer disk become more evident: the left peak wobbles slightly between phases 0.2 and 0.8. The same happens on right peak on phases 0.0-0.4 and 0.6-1.0. At phases 0.5 and 1.0 the bulge towards $-v_x$ can be seen as a warp in the trail, not to be mistaken for the aforementioned wobbling. A weakening in line intensity seen as a shadow can be found leading the bulge. The spiral arm on the opposite side from the bulge can be seen as a faint wave trailing from left to right, and to left again.

4.5 Summary of selected systems

The simulated disks of U Gem and HT Cas are calm and almost featureless. The position maps show a populated inner disk inside 3:2 resonance radius and more variable outer disk. The disk edge stays close to the last non-intersecting resonance orbit and does not have a rotating tail similar to BW Scl and WZ Sge.

The simulated disks of BW Scl and WZ Sge have more features than those of U Gem and HT Cas. Both of the disks have a tail rotating at different pace from the orbital rotation of the binary. The median disk extends beyond the 3:1 and even beyond 2:1 resonance orbit. Spiral arms are visible in the disk. Both disks have a clearly visible dense gas ring just inside 3:2 resonance orbit, with clearly sparser outer disk. However, this is an artefact caused by taking a median over the orbital period - single snapshots of disk at the same phase do not show a remarkably denser area of the disk, but simply the disk inside 3:2 resonance orbit is always populated, while the area outside 3:2 has a rotating tail.

The disk in velocity coordinates is asymmetric. The location where the mass stream hits the disk is clearly visible in the velocity map as a bulge

extending towards negative x- velocity. The spiral arms of position map are visible in velocity map as well. Outer disk velocities follow the last non-intersecting orbit closely, with only little gas falling outside it.

Overall the quiescent disks of all systems presented here are large and close to the last non-intersecting streamline, further confirming that quiescent disks are indeed large and close to truncation limit (Neustroev and Zharikov, 2020), extending even over it.

Chapter 5

Gas velocities of outer disk

Any spatial knowledge on accretion disks are based on either eclipse timing measurements or velocity measurements from spectra. Thus, the knowledge of the velocity fields in accretion disks is crucial to gaining insight of accretion disk structures.

The prevailing accretion disk model, the α-disk model (Shakura and Sunyaev, 1973), assumes a Keplerian velocity field throughout the disk. While widely accepted, it is still unclear if this assumption is actually valid. For example, accretion disk of IP Peg has been studied to be consistent with Keplerian flows (Ishioka et al., 2004) but also have sub-Keplerian velocities along spiral structures (Baptista et al., 2005). Especially the outer disk is expected to have deviations from Keplerian velocities due to its distorted shape.

5.1 Expected Keplerian velocities at tidal truncation radius

Tidal truncation radius (Eq. 2.36) estimates the radius, after which an accretion is truncated due to the tidal dissipation caused by the secondary star. A first estimate of outer disk velocity can be calculated from tidal truncation radius using Eq. 2.38, assuming that the outer disks follows approximately Keplerian flow.

Table 5.1: Characterized radii and velocities of last non-intersecting orbits in units of a and km/s. Additionally, tidal truncation radius and the Keplerian velocity at truncation radius are listed.

System	R_{min}	R_{max}	$\overline{R}$	R_{tru}	V_{min}	V_{max}	$\overline{V}$	$V_{R_{tru}}$
BW Scl	0.49	0.58	0.53	0.58	602	737	670	636
WZ Sge	0.46	0.56	0.51	0.56	634	792	714	674
HT Cas	0.43	0.52	0.47	0.53	537	679	610	573
U Gem	0.36	0.44	0.40	0.45	534	622	581	524

The calculated tidal truncation radii and corresponding Keplerian velocities can be seen in Table 5.1. All systems exhibit lower minimum velocities in their last non-intersecting orbits.

5.2 Outer disk velocities approximated by last non-intersecting orbit

The last non-intersecting orbit gives a reasonably good estimate about the outer disk velocities, as it is thought to give the truncation limit for an accretion disk. Indeed, the velocity maps produced by SPH simulations (Figures 4.11, 4.8, 4.5 and 4.2) show that the last non-intersecting orbit is a good tracer of the outer disk velocities.

For BW Scl (marked with number 1 in equations), the velocity range of last non-intersecting orbit was $V_{out_1} = 600 - 740$ km s^{-1}, with an orbit-averaged value of $\overline{V}_{out_1} = 670$ km s^{-1}. The last non-intersecting orbit of WZ Sge (marked with number 2) had velocity range $V_{out_2} = 635{-}795$ km s^{-1} with an average velocity of $\overline{V}_{out_2} = 715$ km s^{-1}. HT Cas (marked with number 3) had a velocity range of $V_{out_3} = 540 - 680$ km s^{-1} with an average velocity of $\overline{V}_{out_3} = 610$ km s^{-1}, and U Gem (marked with 4) had a velocity range of $V_{out_4} = 534 - 622$ km s^{-1} with an average velocity of $\overline{V}_{out_4} = 581$ km s^{-1}.

The characterised velocities are gathered in Table 5.1. All calculated velocities here have been calculated taking inclination into consideration, causing the un-intuitive 'smaller' velocities of BW Scl compared to WZ Sge. As BW Scl has shorter period and thus smaller accretion disk, its outer disk

velocities without taking inclination into account should be larger than WZ Sge. However, its inclination is 63 degrees, compared to 77 degrees of WZ Sge, causing this contradiction.

5.3 Velocity estimates from reconstructed spectral lines

As shown in Figure 2.4, the radial velocities of an accretion disk edge correspond to the locations of the peaks of double-peaked spectral line. Thus, by measuring the peak positions, one can find the outer disk velocity. In order to do this, the simulated velocity maps and Doppler maps presented in previous chapter were flattened from 2D histograms into 1D histograms with regards to the x-axis.

In theory, as the disk rotates, the lines should move relative to each other due to the oval shape of the outer disk in velocity space. To check if this could be seen in any of our simulated or observed spectra, two different 1D histograms were constructed: one at phase 0.0, where the narrowest side of the disk is facing the x-axis, and another at phase 0.25 where the outer disk is at its widest with respect to the x-axis.

Figure 5.1 shows reconstructed spectral lines of all four systems. For SPH simulated data, 3 line profiles are shown: orbit-averaged, and line profiles at phases 0 and 0.25. Additionally, orbit-averaged spectral line from observational data is shown for WZ Sge and U Gem. Since the Doppler maps for HT Cas and BW Scl were ready-made, no spectral line data was available. All the measured velocities are found in Table 5.2.

BW Scl and WZ Sge show a wider line profile compared to HT Cas and U Gem. This is most likely due to the obvious bulge seen in simulated velocity maps in Figures 4.11 and 4.8. U Gem has a noticeably different line shape compared to the others: peaks are sharp and the line then widens concavely towards the wings. This corresponds to the particles consentrating heavily on the outer disk, as can be seen in Figure 4.2.

Measuring from peak-to-peak separation of the line profile, the outer disk

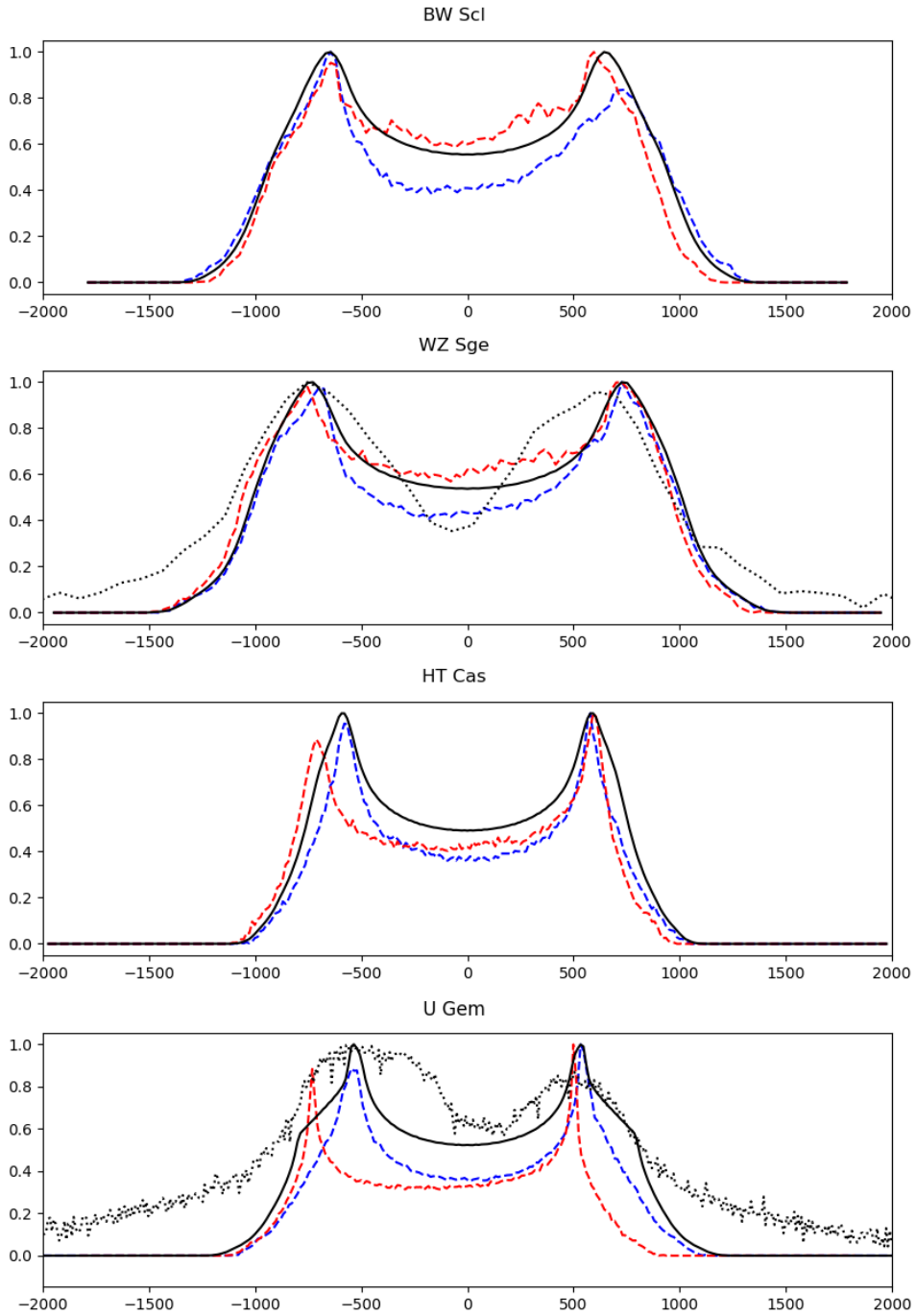

Figure 5.1: Flattened 1D histograms, depicting spectral lines. Black, solid line portrays orbit-averaged line; red dashed line is at phase P=0; and blue dashed line is at P=0.25. For WZ Sge and U Gem orbit-averaged H_α line from observational data is presented with black dotted line.

velocity of simulated disk of BW Scl is between 620-702 km/s, with orbital average at 650 km/s ± 35 km/s. A conservative 5% accuracy is assumed here, due to the subjective measurement by hand. The velocity range fits well inside the range given by last non-intersecting orbit, with smaller average velocity. The observed minimum velocity of the system is 635 km/s (Neustroev and Mäntynen, 2022), corresponding well to the calculated Keplerian velocity at the truncation radius.

For WZ Sge, the corresponding outer disk velocity range is 701-740 km/s, with an orbit-averaged outer disk velocity of 727 ± 35 km/s. The outer disk velocity measured from the observed H_α line is 680 km/s ± 35 km/s. Contrary to BW Scl, the orbit-averaged outer disk velocity is actually higher than than the average velocity of last non-intersecting streamline. This difference could be caused by BW Scl having slightly denser areas around the outer disk, particularly on the area trailing the bulge, while also having outer disk extend more past the last non-intersecting orbit.

The bulges of the accretion disk in both BW Scl and WZ Sge make the outer disk velocity measurements using line profiles at least somewhat unreliable. By looking at the velocity map of Figures 4.11 and 4.8, the lower maximum velocities resulting from peak-to-peak distance measurements compared to last non-intersecting orbit velocities can be understood. The accretion disk extends over last non-intersecting orbit. However, the minimum velocity measured from the line profile should be around the minimum velocity of the last non-intersecting orbit, or even a little bit slower, which is not the case. Clearly the bulge widens the peak-to-peak separation.

Velocity range of the simulated outer accretion disk of HT Cas is 580-652 km/s, with orbital average of 586±30 km/s. Compared, Neustroev and Zharikov (2020) measured the outer disk velocity from H_α line to be 575 ± 4 km/s. All the velocities fit inside the range given by last non-intersecting orbit; however, the velocity range given by the simulated line profile is smaller than expected, as the disk in Figure 4.5 overflows only slightly past the non-intersecting orbit and there are no significant distortions in the velocity map. Most likely the bulk of the line profile peaks come from the more dense areas corresponding roughly to 3:1 resonance orbit, making the minimum end of the

Table 5.2: Outer disk velocities measured from line profiles in km/s. Presented are the minimum velocity V_{min} at P=0.25, maximum velocity V_{max} at P=0.0, orbital average of simulated line profile $\overline{V}$ and orbital average of outer disk velocity measured from H_α emission line.

System	V_{min}	V_{max}	$\overline{V}$	$\overline{V}_{obs}$
BW Scl	620	702	650	635
WZ Sge	701	740	727	680
HT Cas	580	652	586	575
U Gem	533	615	533	531

velocity range larger than that predicted by last non-intersecting streamline; while the overflow in the first quadrant makes the maximum end of the range depict smaller than expected velocities.

For U Gem, the velocity range is 533-615 km/s, coinciding quite well with the last non-intersecting streamline velocity range. Orbit-averaged velocity is 533 ± 25 km/s. The velocity measured from observational data is 531 ± 30 km/s. The error margin here is quite large, since the bright spot visible in Figure 4.1 causes the left peak to be quite broad, making it difficult to differentiate the disk emission from the bright spot emission and recognise the peak position.

5.4 Is Keplerian disk a valid assumption?

It seems that for all presented systems, the Keplerian velocity at tidal truncation radius gives a solid lower limit for orbit-averaged disk velocity, as orbit-averaged velocities given by both last non-intersecting streamline calculations and simulated line profiles are larger than the velocities at tidal truncation limit. The velocity deviations found in both last non-intersecting orbits and line profile measurements are large, even over 100 km/s, but mostly cancel each other during the orbital period.

For BW Scl and WZ Sge, the line profiles constructed from SPH simulations are not trustworthy for estimating outer edge velocity due to the deviations in outer disk structure. Truss (2007) already noted that disks in small mass ratio systems ($q \leq 0.1$) have disks that fill most of their Roche

lobe, while turning so that their elongation is almost perpendicular to that of the last non-intersecting orbit. This is also observed in simulations done for WZ Sge and BW Scl; however, it is not visible in the velocity maps of this thesis as low-density regions have been ignored by taking median over the orbital period and not mean. Truss (2007) also noted, that the assumed temperature profile given as a parameter to the SPH code changes the disk structure in these small mass ratio environments. Thus, altering the temperature profile of the simulation might provide slightly different disks, from which better estimates could be made. Aside from this, it should be noted that the outer disk velocities do follow the last non-intersecting orbit quite closely outside the bulge area.

Another shortcoming is the used method for measuring the line peak positions. The positions were measured by hand, estimating the location visually. A more precise method would be fitting a double-Gaussian to the line profile and measuring the peaks that way; however, the measurements here were done only for estimates of the velocities, and thus, using more complicated method would have been out of scope for this thesis. Emissivity distribution over the accretion disk should also change the emission line shape, but in this thesis it was not taken into account.

Comparing the velocity measurements from H_α line to the truncation limit velocities give a clear indication that all four systems do have a large accretion disk, extending up to the truncation limit. Orbital averages of simulated line profiles of HT Cas and especially U Gem give the same conclusion.

The measurements, simulations, and observational data presented here conclude, that:

1. The last non-intersecting orbit seems to trace the truncation limit quite well. Although deviations exist, they are small and thus this easily calculated orbit can be used as an estimate for the disk edge even in small mass-ratio systems.

2. Deviations in velocity caused by the secondary star do cancel out when averaging over orbital period, and circular Keplerian velocities in outer disk can be assumed when considering orbit-averaged data.

3. Keplerian velocity at tidal truncation radius gives a solid lower limit to outer edge velocity.

However, with systems of low mass ratio, more study needs to be done, especially taking the low density regions in the outer disk and the rotating 'tail' of the disk into account. In that case, the gas flows beyond the last non-intersecting orbit, and based on this study its behaviour and velocity profile is left unclear.

Chapter 6

Acknowledgements

We acknowledge with thanks the variable star observations from the AAVSO International Database contributed by observers worldwide and used in this research

This thesis makes use of data obtained from the Isaac Newton Group Archive which is maintained as part of the CASU Astronomical Data Centre at the Institute of Astronomy, Cambridge.

Based on observations collected at the European Southern Observatory under ESO programme 078.D-0448(A).

Bibliography

Augusteijn, T. and Wisotzki, L. (1997). HE 2350-3908: a dwarf nova with a 78m̂ôrbital period. A&A, 324:L57–L60.

Balbus, S. A. and Hawley, J. F. (1991). A Powerful Local Shear Instability in Weakly Magnetized Disks. I. Linear Analysis. ApJ, 376:214.

Baptista, R., Morales-Rueda, L., Harlaftis, E. T., Marsh, T. R., and Steeghs, D. (2005). Tracing the spiral arms in IP Pegasi. A&A, 444(1):201–211.

Cannizzo, J. K. (1993). The Accretion Disk Limit Cycle Model: Toward an Understanding of the Long-Term Behavior of SS Cygni. ApJ, 419:318.

Cannon, A. J. (1907). Second catalogue of variable stars. *Annals of Harvard College Observatory*, 55:1–94.

Cash, J. and Karp, A. (1990). A variable order runge—kutta method for value problems with rapidly varying right-hand sides. *ACM Trans. Math. Softw.*, 16:201–222.

Dekker, H., D'Odorico, S., Kaufer, A., Delabre, B., and Kotzlowski, H. (2000). Design, construction, and performance of UVES, the echelle spectrograph for the UT2 Kueyen Telescope at the ESO Paranal Observatory. In Iye, M. and Moorwood, A. F., editors, *Optical and IR Telescope Instrumentation and Detectors*, volume 4008 of *Society of Photo-Optical Instrumentation Engineers (SPIE) Conference Series*, pages 534–545.

Echevarría, J., de la Fuente, E., and Costero, R. (2007). U Geminorum: A Test Case for Orbital Parameter Determination. AJ, 134(1):262–273.

Eggleton, P. P. (1983). Aproximations to the radii of Roche lobes. ApJ, 268:368–369.

Flebbe, O., Muenzel, S., Herold, H., Riffert, H., and Ruder, H. (1994). Smoothed Particle Hydrodynamics: Physical Viscosity and the Simulation of Accretion Disks. ApJ, 431:754.

Frank, J., King, A., and Raine, D. J. (2002). *Accretion Power in Astrophysics: Third Edition.*

Fromang, S. and Papaloizou, J. (2007). MHD simulations of the magnetorotational instability in a shearing box with zero net flux. I. The issue of convergence. A&A, 476(3):1113–1122.

Gingold, R. A. and Monaghan, J. J. (1977). Smoothed particle hydrodynamics: theory and application to non-spherical stars. MNRAS, 181:375–389.

Goldreich, P. and Tremaine, S. (1978). The excitation and evolution of density waves. ApJ, 222:850–858.

Hernandez Santisteban, J. V. (2021). PyDoppler: Wrapper for Doppler tomography software.

Hessman, F. V. and Hopp, U. (1990). The massive, nearly face-on cataclysmic variable GD 552. A&A, 228:387–398.

Hind, J. R. (1856). On a new Variable Star. MNRAS, 16:56–56.

Hoffmeister, C. (1943). 213 neue Veränderliche. *Astronomische Nachrichten*, 274:36.

Horne, K. (1985). Images of accretion discs -I. The eclipse mapping method. MNRAS, 213:129–141.

Horne, K., Wood, J. H., and Stiening, R. F. (1991). Eclipse Studies of the Dwarf Nova HT Cassiopeiae. I. Observations and System Parameters. ApJ, 378:271.

Ishioka, R., Mineshige, S., Kato, T., Nogami, D., and Uemura, M. (2004). Line-Profile Variations during an Eclipse of a Dwarf Nova, IP Pegasi. PASJ, 56:481–485.

Ju, W., Stone, J. M., and Zhu, Z. (2017). Global MHD Simulations of Accretion Disks in Cataclysmic Variables (CVs). II. The Relative Importance of MRI and Spiral Shocks. ApJ, 841(1):29.

Kotko, I. and Lasota, J. P. (2012). The viscosity parameter α and the properties of accretion disc outbursts in close binaries. A&A, 545:A115.

Kotze, E. J., Potter, S. B., and McBride, V. A. (2015). Exploring inside-out Doppler tomography: non-magnetic cataclysmic variables. A&A, 579:A77.

Landau, L. D. and Lifshitz, E. M. (1987). *Fluid Mechanics*.

Lasota, J.-P. (2001). The disc instability model of dwarf novae and low-mass X-ray binary transients. New A Rev., 45(7):449–508.

Liu, G. T. and Liu, M. B. (2003). *Smoothed particle hydrodynamics — a meshfree particle method*.

Lubow, S. H. (1991). A Model for Tidally Driven Eccentric Instabilities in Fluid Disks. ApJ, 381:259.

Lubow, S. H. and Shu, F. H. (1975). Gas dynamics of semidetached binaries. ApJ, 198:383–405.

Makita, M., Miyawaki, K., and Matsuda, T. (2000). Two- and three-dimensional numerical simulations of accretion discs in a close binary system. MNRAS, 316(4):906–916.

Marsh, T. R. and Horne, K. (1988). Images of accretion discs - II. Doppler tomography. MNRAS, 235:269–286.

Monaghan, J. J. (1992). Smoothed particle hydrodynamics. ARA&A, 30:543–574.

Monaghan, J. J. and Gingold, R. A. (1983). Shock Simulation by the Particle Method SPH. *Journal of Computational Physics*, 52(2):374–389.

Monaghan, J. J. and Lattanzio, J. C. (1985). A refined particle method for astrophysical problems. A&A, 149(1):135–143.

Neustroev, V. and Mäntynen, I. (2022). Detection of the brown dwarf donor in the period-bouncer BW Sculptoris. *arXiv e-prints*, page arXiv:2212.03264.

Neustroev, V. V., Suleimanov, V. F., Borisov, N. V., Belyakov, K. V., and Shearer, A. (2011). Dark spot, spiral waves and the SW Sextantis behaviour: it is all about UX Ursae Majoris. MNRAS, 410(2):963–977.

Neustroev, V. V. and Zharikov, S. V. (2020). Voracious vortices in cataclysmic variables. II. Evidence for the expansion of accretion disc material beyond the Roche lobe of the accretor in HT Cassiopeia during its 2017 superoutburst. A&A, 642:A100.

Paczynski, B. (1977). A model of accretion disks in close binaries. ApJ, 216:822–826.

Papaloizou, J. C. B. and Lin, D. N. C. (1995). Theory Of Accretion Disks I: Angular Momentum Transport Processes. ARA&A, 33:505–540.

Patterson, J. (1981). Rapid oscillations in cataclysmic variables. VI. Periodicities in erupting dwarf novae. ApJS, 45:517–539.

Sawada, K., Matsuda, T., and Hachisu, I. (1986). Spiral shocks on a Roche lobe overflow in a semi-detached binary system. MNRAS, 219:75–88.

Shakura, N. I. and Sunyaev, R. A. (1973). Reprint of 1973A&A....24..337S. Black holes in binary systems. Observational appearance. A&A, 500:33–51.

Skidmore, W., Mason, E., Howell, S. B., Ciardi, D. R., Littlefair, S., and Dhillon, V. S. (2000). Investigating the structure of the accretion disc in WZ Sge from multiwaveband time-resolved spectroscopic observations - I. MNRAS, 318(2):429–439.

Smak, J. and Waagen, E. O. (2004). The 1985 Superoutburst of U Geminorum. Detection of Superhumps. Acta Astron., 54:433–442.

Sorathia, K. A., Reynolds, C. S., Stone, J. M., and Beckwith, K. (2012). Global Simulations of Accretion Disks. I. Convergence and Comparisons with Local Models. ApJ, 749(2):189.

Spruit, H. C. (1998). Fast maximum entropy Doppler mapping. *arXiv e-prints*, pages astro–ph/9806141.

Stauffer, J., Spinrad, H., and Thorstensen, J. (1979). Spectra of the M dwarf companion in U Geminorum. PASP, 91:59–61.

Steeghs, D., Howell, S. B., Knigge, C., Gänsicke, B. T., Sion, E. M., and Welsh, W. F. (2007). Dynamical Constraints on the Component Masses of the Cataclysmic Variable WZ Sagittae. ApJ, 667(1):442–447.

Sulkanen, M. E., Brasure, L. W., and Patterson, J. (1981). Accretion disk radii in cataclysmic variables. ApJ, 244:579–581.

Szkody, P. and Mattei, J. A. (1984). Analysis of the AAVSO light curves of 21 dwarf novae. PASP, 96:988–995.

Truss, M. R. (2007). Accretion disc dynamics in extreme mass ratio compact binaries. MNRAS, 376(1):89–97.

Warner, B. (2003). *Cataclysmic Variable Stars*.

Wood, J. H., Naylor, T., Hassall, B. J. M., and Ramseyer, T. F. (1995). The discovery of an X-ray eclipse during a low state of the dwarf nova HT Cassiopeiae. MNRAS, 273(3):772–784.

Yukawa, H., Boffin, H. M. J., and Matsuda, T. (1997). Spiral shocks in three-dimensional accretion discs. MNRAS, 292(2):321–330.

Zhang, E. H., Robinson, E. L., and Nather, R. E. (1986). The Eclipses of Cataclysmic Variables. I. HT Cassiopeiae. ApJ, 305:740.